

Spontaneous Formation of an Internal Shear Band in Ice Flowing over Topographically Variable Bedrocks

Emma Liu¹, Ludovic Räss¹, Yury Podladchikov², Frédéric Herman³, and Jenny Suckale^{3,4}

¹Affiliation not available

²Institute of Earth Sciences, University of Lausanne

³Institute of Earth Surface Dynamics, University of Lausanne

⁴Geophysics Department, Stanford University

May 27, 2023

Spontaneous Formation of an Internal Shear Band in Ice Flowing over Topographically Variable Bedrocks

Emma Weijia Liu¹, Ludovic Räss^{2,3}, Frédéric Herman⁴, Yury Podladchikov⁵,
Jenny Suckale¹

¹Geophysics Department, Stanford University, USA

²Laboratory of Hydraulics, Hydrology and Glaciology (VAW), ETH Zurich, Switzerland

³Swiss Federal Institute for Forest, Snow and Landscape Research (WSL), Switzerland

⁴Institute of Earth Surface Dynamics, University of Lausanne, Switzerland

⁵Institute of Earth Sciences, University of Lausanne, Switzerland

Key Points:

- Ice flowing over rough basal topography may spontaneously develop an internal shear band on topographic highs.
- Two competing mechanisms control the energy balance near the bedrock: vertical advective cooling and internal shear heating.
- We summarize how basal topography and the rheological power-law exponent influence shear band formation in a regime diagram.

Corresponding author: Emma Weijia Liu, liuwj@stanford.edu

Abstract

Ice surface speed increases dramatically from upstream to downstream in many ice streams and glaciers. This speed-up is thought to be associated with a transition from internal, distributed deformation to highly localized deformation at the ice-bedrock interface. The physical processes governing this transition remain unclear. Here, we argue that basal topography can give rise to internal shear localization. The power-law rheology exponent n amplifies the feedback between shear heating and localization, leading to the spontaneous formation of an internal shear band that creates flow separation within the ice. We model the thermo-mechanical ice flow over a sinusoidal basal topography by building on the high-resolution Stokes solver FastICE v1.0. To capture the interactions between ice and rock, we implement an Immersed Boundary Method and use a level-set approach to represent the free surface of the ice. We compile a regime diagram summarizing when a sinusoidal topography with a given amplitude and wavelength lead to shear band formation for a given rheology. We compare our model results to borehole measurements from Greenland and find evidence that supports the existence of a shear band.

Plain Language Summary

On its way towards the ocean, ice speeds up dramatically from less than one meter per year inland to more than a kilometer per year downstream. In this paper, we investigate the physical processes controlling this speed-up. More specifically, we focus on the role that the bedrock topography underneath the ice and the rheology might play to facilitate this transition. We use a two-dimensional numerical model to simulate the flow field within a slab of ice flowing down a ramp over a simplified topography. We find that including basal topography can lead to a zone of highly localized deformation within the ice above topographic highs. We compare our model results to borehole measurements from Greenland and find evidence that supports the existence of a shear band.

1 Introduction

The world's two largest ice sheets, Antarctica and Greenland, discharge most of their ice mass through fast-moving ice stream and mountain glaciers (Joughin et al., 2010; Rignot et al., 2011). On its path toward the ocean, ice initially moves at relatively low speeds of about one meter per year (Rignot et al., 2011), but then speeds up dramatically reaching surface speeds more than a kilometer per year in some ice stream and glaciers (Rignot et al., 2002; Joughin et al., 2003; Mouginot et al., 2014). The speed-up is thought to be associated with a transition from flow through internal, distributed deformation to sliding, accommodated by highly localized deformation at the ice-bedrock interface (Clarke, 1987; Whillans et al., 1987). This transition from slow flow inland to rapid sliding in outlets is known as the flow-to-sliding transition.

One potential explanation for the flow-to-sliding transition is thawing of the bed, since ice moving over a temperate bed can slide while ice frozen onto the bed must deform internally. The creep instability could facilitate thawing (Robin, 1955) because deformation is most pronounced in cold ice near the bed, leading to shear weakening and intensified deformation until temperature reaches the pressure melting point (Clarke et al., 1977; Yuen & Schubert, 1979). However, it remains unclear how viable this explanation is, as first mentioned in Nye (1971) and later substantiated by Larson (1980) and Fowler (2001) who showed that the local conservation of flux implies a reduction in shearing, translating into less energy release and refreezing. Bueler (2009) identified the advection of cold ice to the warm bed as the main impediment for a sudden transition to sliding; an argument further developed by Mantelli et al. (2019).

The work by Bueler (2009) and Mantelli et al. (2019) suggests that the flow-to-sliding transition does not happen suddenly, but gradually over an extended distance in the flow

66 direction. What are the physical processes governing this transition and the scale over
67 which it occurs? Clues come from borehole measurements (Lüthi et al., 2002; Ryser et
68 al., 2014; Harrington et al., 2015; Hills et al., 2017; Doyle et al., 2018; Maier et al., 2019;
69 Law et al., 2023) suggest a complex, depth-dependent velocity field in the ice above a
70 topographically variable bed. Many factors may contribute to this variability, including
71 the presence of sediments and sediment-freeze-on (Herron et al., 1979; Gow et al., 1979;
72 Goodwin, 1993; Carsey et al., 2002), subglacial hydrology (Doyle et al., 2018), seasonal
73 cycles (Ryser et al., 2014), paleo history (Lüthi et al., 2002), and variable topography
74 (Law et al., 2023). Here, we focus specifically on the role of variable topography as a first
75 step towards a more complete understanding.

76 The goal of this paper is to understand the impact of topographically uneven hard
77 bedrock on ice flow acceleration by quantifying shear localization in the vicinity of the
78 bedrock using numerical simulations. Several prior studies have investigated the role of
79 topography on the thermo-mechanical deformation of sliding ice (e.g., Gudmundsson,
80 1997; Helanow et al., 2020, 2021). Our work complements these existing contributions
81 by focusing on flowing ice, prior to the onset of sliding. We hypothesize that the intense
82 deformation of cold ice flowing over sufficiently pronounced basal topography can lead
83 to the formation of an internal shear band connecting topographic highs that accounts
84 for most of the internal deformation within the ice. Similarly to flow separation in slid-
85 ing ice (Gudmundsson, 1997), we expect that the conditions for shear band formation
86 depend on both the topography imposed and the rheology imposed, most notably the
87 degree of non-linearity embedded into the rheology through the power-law exponent n .

88 We test our hypothesis through numerical simulations, building on recent advances
89 in simulating the thermo-mechanical deformation of ice at high resolution implemented
90 in FastICE v1.0 (Räss et al., 2020). We add to the original release of FastICE v1.0 by
91 incorporating a free surface and variable basal topography since both are critical for the
92 physical process that we aim to understand. We capture the free ice surface using a level-
93 set representation (Osher & Sethian, 1988; Sethian & Smereka, 2003) and the basal to-
94 pography through an Immersed-Boundary Method (Peskin, 1972, 2002). The deforma-
95 tion of ice depends sensitively on ice rheology, because different rheology formulations
96 can imply orders of magnitude differences in the response of ice deformation to stresses.
97 To gain insights into the influence of rheology on shear band formation, specifically the
98 rheological power-law exponent n , we also consider different values of exponent from $n =$
99 1 to $n = 4$.

100 Recently, Law et al. (2023) provides compelling evidence for complex, depth-dependent
101 ice motion for three glaciers in Greenland, Sermeq Kujalleq/Store Glacier and Isunnguata
102 Sermia Glacier, consistent with the idea of flow separation by Gudmundsson (1997). By
103 linking field observations and numerical simulations, Law et al. (2023) show that both
104 the vertical extent of temperate ice near the bed and the portion of deformation accom-
105 modated by basal slip varies significantly at the field-site scale and call for an improved
106 parametrization of this variability in ice-sheet models. They also show that mostly used
107 bedrock topography such as BedMachine (Morlighem et al., 2017) is too coarse and smooth.
108 Thus using geostatistically more accurate realisation of bedrock topography results in
109 rougher bedrock and enhanced shear localization. Deriving an improved parameteriza-
110 tion requires an improved understanding of the physical processes governing the observed
111 complexities in depth-dependent ice motion. We intentionally focus on an idealized si-
112 nusoidal topography to advance this process-based understanding. We synthesize our sim-
113 ulation results into a regime diagram that summarizes how the formation of an inter-
114 nal shear band depends on both the amplitude and wavelength of the underlying topog-
115 raphy and on the assumed ice rheology.

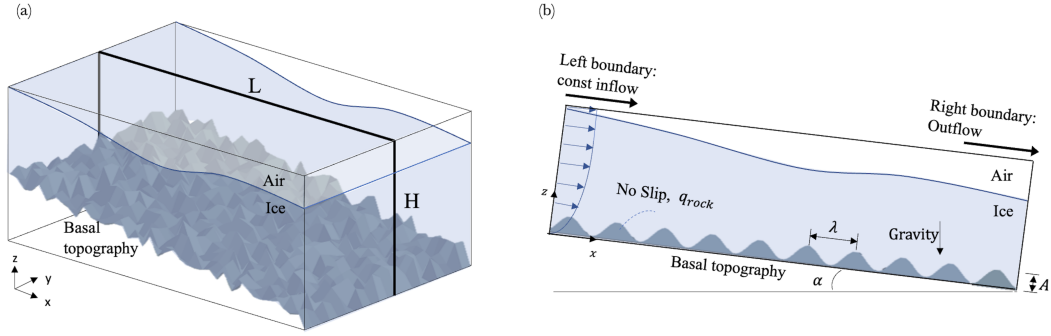


Figure 1. Model geometry of ice sheet flowing over rough hard bedrock. (a) The general case of a slab of ice flowing over rough hard bedrock in three-dimensions with a free surface. (b) The two-dimensional model setup with a sinusoidal basal topography and a free surface.

2 Methods

116

117 To approximate the thermo-mechanical deformation within a slab of ice flowing over
 118 a rough hard bedrock in the downstream direction x (Figure 1, a), we neglect variabil-
 119 ity in the transverse direction y . This choice reduces our modeling domain to a two-dimensional,
 120 along-flow cut through the three-dimensional ice slab along the thick black line (Figure
 121 1, a). The depth direction z is oriented vertically upwards from the bedrock. The origin
 122 of the axes ($x = 0, z = 0$) locates at the bedrock of the flow inlet. The size of the
 123 model domain is $(0, L) \times (0, H)$, and it is tilted at an angle α . To represent basal topog-
 124 pography, we adopt an idealized sinusoidal contour $z = A \sin(kx)$ with an amplitude
 125 A and a wavenumber k . We include a thin layer of low-viscosity phase on top of the ice
 126 to mimic the presence of air, which allows ice thickness to change spatially and tempo-
 127 rally.

128 We capture the depth-dependent thermo-mechanical ice deformation implement-
 129 ing an incompressible viscous Stokes solver using the time-dependent implicit pseudo-
 130 transient methods and the finite difference discretization (Räss et al., 2020; Räss et al.,
 131 2022). To prescribe the basal ice-bedrock boundary condition, we implement the Immersed
 132 Boundary Method, a fictitious domain method that allows to treat fluid and structural
 133 domains separately (Peskin, 1972, 2002). To incorporate the free surface boundary con-
 134 dition, we use the level-set Methods, an implicit description for moving fronts further
 135 advected with the local fluid velocity (Sethian & Smereka, 2003; Osher et al., 2004). The
 136 implementations of ice-bedrock and ice-air boundary condition are discussed in Section
 137 2.2.

2.1 Thermo-mechanical Model

138

139 We describe ice as an incompressible, non-linear, viscous fluid with a temperature-
 140 dependent rheology. The momentum equations are

$$141 \quad \frac{\partial \tau_{ij}}{\partial x_j} - \frac{\partial p}{\partial x_i} + F_i = 0, \quad \tau_{ij} = 2\eta \dot{\epsilon}_{ij}, \quad (1)$$

142 where $F_i = \rho g(\sin \alpha, \cos \alpha)$ is the gravitational body force at a tilted angle α , p is isotropic
 143 pressure, τ_{ij} is the deviatoric stress tensor, $\dot{\epsilon}_{ij}$ is the shear strain rate tensor, and η is
 144 the ice viscosity. Reducing the model to two dimensions implies that all components in
 145 the transverse direction y are zero. The only non-zero shear strain rate and shear stress
 146 are $\dot{\epsilon}_{zx}$ and τ_{zx} , respectively.

147 Ice flows into the domain from the left boundary over an undeforming hard bedrock,
 148 and exits at the right boundary. We calculate the analytical inflow field by solving the
 149 momentum balance along the flow at steady state

$$150 \quad \eta(z) \frac{\partial u}{\partial z} = \rho g (H - z) \sin \alpha, \quad \eta(z) = \eta_b + (\eta_s - \eta_b) \frac{z}{H}, \quad (2)$$

151 where we assume a linear viscosity profile between the viscosity at the bed, η_b , and the
 152 viscosity at the surface, η_s . Integrating equation (2), we have the analytical inflow ve-
 153 locity

$$154 \quad u_{\text{inlet}} = \frac{\rho g \sin \alpha}{K^2} [\eta_b \log(\eta_b + Kz) + KH \log(\eta_b + Kz) - Kz] + C, \quad (3)$$

155 where $K = (\eta_s - \eta_b)/H$, and C is the integration constant such that the velocity at
 156 bed is zero. When viscosity is constant throughout the domain, $\eta_s = \eta_b = \eta_0$, the an-
 157 alytical inflow velocity simplifies to a parabolic velocity profile $u_{\text{inlet}} = \rho \sin \alpha / \eta_0 (Hz -$
 158 $0.5z^2)$.

159 At the outlet, we adapt the outflow boundary condition from Orlanski (1976)

$$160 \quad \frac{\partial u}{\partial t} + U \frac{\partial u}{\partial x} = 0, \quad (4)$$

161 where U is the propagation velocity. Following the approach by Kreiss (1968), we esti-
 162 mate it numerically by calculating the propagation velocity between neighboring grid points
 163 $U = \Delta x / \Delta t$, where Δx and Δt are the spatial and temporal grid sizes, respectively.
 164 The extrapolated velocity at the outlet boundary is then

$$165 \quad u_{n_x}^{n_t} = 2u_{n_x-1}^{n_t-1} - u_{n_x-2}^{n_t-2}, \quad (5)$$

166 where n_x is the boundary point and n_t is the current time step.

167 At the ice surface, we assume that the atmospheric pressure is negligible relative
 168 to the pressure in the ice column, implying a stress-free surface

$$169 \quad \sigma_{ij} n_j = 0, \quad (6)$$

170 where n_j is the normal vector to the ice surface, σ_{ij} is the Cauchy stress tensor, obtained
 171 by combining the isotropic pressure p and the deviatoric stress τ_{ij} . In addition, we im-
 172 pose a constant atmospheric temperature at ice surface $T_s = -26^\circ\text{C}$.

173 At the ice-bedrock interface, we assume ice is frozen to bed and impose a no-slip
 174 boundary condition. We implement this boundary condition using the Immersed Bound-
 175 ary Methods. In addition, we impose a constant geothermal heat flux of $0.05\text{W}/\text{m}^2$ (Wright
 176 et al., 2012; Shapiro & Ritzwoller, 2004; Maule et al., 2005). The details are discussed
 177 in Section 2.2.

178 The thermal model takes into account the effects of diffusion, advection, shear heat-
 179 ing, and melt water weakening. We curtail the temperature at $T_m = -0.1^\circ\text{C}$ and es-
 180 timate the melt rate with the latent heat. The energy equation is given by

$$181 \quad \rho c_p \left(\frac{\partial T}{\partial t} + u_i \frac{\partial T}{\partial x_i} \right) = \frac{\partial}{\partial x_i} \left(\kappa \frac{\partial T}{\partial x_i} \right) + 2\tau_E \dot{\epsilon}_E - L\dot{m}, \quad (7)$$

182 where c_p is the specific heat of ice, κ is the thermal conductivity, τ_E and $\dot{\epsilon}_E$ are effec-
 183 tive shear stress and effective shear strain rate, respectively. The term $2\tau_E \dot{\epsilon}_E$ represents
 184 shear heating, $L\dot{m}$ captures the energy required for melting where $L = 0.366 \times 10^6 \text{J}/\text{kg}$
 185 is the latent heat, and \dot{m} is the generated melt water flux.

186 In the temperate zone where temperature is around the melting point, as defined
 187 by the logistic function

$$188 \quad f(T - T_m) = 1 - \tanh(-0.5(T - T_m)), \quad (8)$$

189 we assume that the shear heating $2\tau_E\dot{\epsilon}_E$ is absorbed for the phase change from ice to
 190 water (Suckale et al., 2014; Räss et al., 2020). The temperature in the temperate zone
 191 can hence not exceed the pressure melting point, leading to the simplified energy equa-
 192 tion

$$193 \quad \rho c_p \left(\frac{\partial T}{\partial t} + u_i \frac{\partial T}{\partial x_i} \right) = \frac{\partial}{\partial x_i} \left(\kappa \frac{\partial T}{\partial x_i} \right) + 2\tau_E \dot{\epsilon}_E f(T - T_m). \quad (9)$$

194 The logistic function (8) serves as an indicator of how close the ice temperature is to the
 195 melting point T_m . When the temperature has reached the melting point, i.e., $f(T - T_m) =$
 196 0 , all shear heating is absorbed to for the phase change from ice to water, and no net heat
 197 source is added to energy equation.

198 The time dependence of the problem comes from the free surface evolution and from
 199 the energy equation because the shear heating, diffusion and advection terms are tran-
 200 sient. At each physical time step, we use the pseudo-transient method (Räss et al., 2022)
 201 to solve the system of coupled momentum equation (1) and energy equation (9) itera-
 202 tively until the continuity residual, $\partial p / \partial \tau_p$, momentum residual, $\partial u_i / \partial \tau_u$, and temper-
 203 ature residual, $\partial T / \partial \tau_T$, are minimized, achieving an implicit solution of the equations.
 204 Thus, the governing equations in a residual form are

$$205 \quad \frac{\partial p}{\partial \tau_p} = -\frac{\partial u_i}{\partial x_i}, \quad (10)$$

$$206 \quad \frac{\partial u_i}{\partial \tau_u} = \frac{\partial \tau_{ij}}{\partial x_j} - \frac{\partial p}{\partial x_i} + F_i, \quad (11)$$

$$207 \quad \frac{\partial T}{\partial \tau_T} = -\frac{\partial T}{\partial t} - u_i \frac{\partial T}{\partial x_i} + \frac{1}{\rho c_p} \left(\frac{\partial}{\partial x_i} \left(\kappa \frac{\partial T}{\partial x_i} \right) + 2\tau_E \dot{\epsilon}_E f(T - T_m) \right), \quad (12)$$

208 where τ presents the pseudo time step, and t represents physical time step.

209 The key limiting factor of the convergence rates of equations (10) to (12) is the con-
 210 vergence rate of the ice viscosity. During iterations in pseudo time, we do not evolve the
 211 ice surface. After the residuals fall below the defined thresholds indicating that the nu-
 212 merical solution has reached steady state, we advect the free surface with the local ice
 213 velocity. The details of the advection of the free surface is presented in Section 2.2.

214 We adopt a power-law relationship for the rheology model and specifically inves-
 215 tigate the power-law with different values of the exponent n

$$216 \quad \dot{\epsilon}_{ij} = a \tau_{II}^{n-1} \exp \left(-\frac{Q}{R(T_s + T)} \right) \tau_{ij}, \quad (13)$$

217 where a is pre-factor, Q the activation energy, R the universal gas constant, and T_s the
 218 surface temperature.

219 One challenge in implementing the power-law rheology is that the pre-factor a is
 220 difficult to constrain experimentally or observationally, partly because it captures sev-
 221 eral different physical processes, such as grain size, temperature, fabrics, and other vari-
 222 ables (Paterson, 1994).

223 In our model, a depends only on temperature and interstitial water content, and
 224 we neglect other dependencies mostly because limited data exists to constrain these. The
 225 temperature dependency is described as Arrhenius relationship in equation (13). To cap-
 226 ture the viscosity-weakening effect of interstitial water, we define an additional param-
 227 eter a_w . In our model, we use the same logistic function from equation (8) that reads
 228 $a_w = (1 - f(T - T_m))$ in the energy equation to capture viscous weakening in the pres-
 229 ence of water for the power-law (Suckale et al., 2014). Thus, our implementation of the
 230 pre-factor is $a = a_0 a_w$, where a_0 is treated as constant and comes from other depen-
 231 dencies such as grain size and fabrics.

232 It is important to note that interstitial water can impact not only the pre-factor
 233 a , but also the exponent n . Recent research by Adams et al. (2021) suggests that the

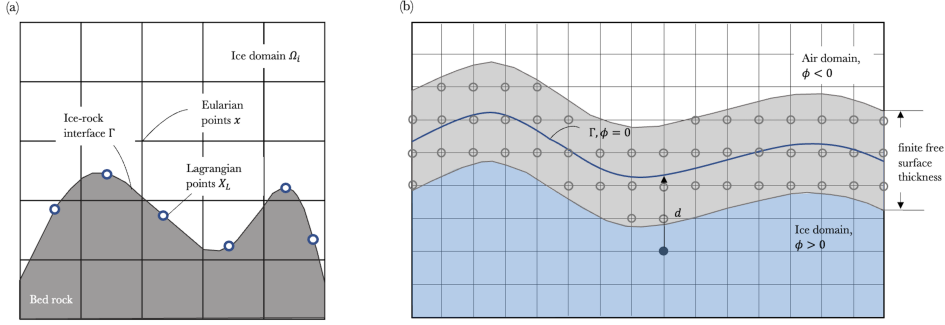


Figure 2. Illustration of Immersed Boundary Method and level-set Method. (a): Treatment of the ice-bedrock interface. The spatial discretization of the ice domain, Ω_i , and bed shape, Γ . Ω_i is discretized in a Cartesian grid x . The ice-bedrock interface, Γ , is discretized using Lagrangian points X_L . (b): Treatment of the ice-air interface. The domain is divided into ice (blue) and air (white) domains using a level-set function with a finite but very small free surface thickness (light grey) of $3\Delta x$.

234 exponent for temperate ice with sufficient interstitial water is close to 1.1. Other studies
 235 have also found similar enhancements in creep rates as ice approaches pressure melt-
 236 ing point (e.g., Mellor & Testa, 1969; Barnes, Tabor, & Walker, 1971). However, due to
 237 limited data to accurately constrain the effect of interstitial water on the value of n , our
 238 model does not consider this impact.

239 2.2 Implementation of the Basal Interface and Free Surface

240 To simulate the mechanical and thermal interactions along the ice-bedrock inter-
 241 face Γ , we integrate the Immersed Boundary Method (IBM) (Peskin, 1972, 2002) into the
 242 Stokes solver. IBM is a fictitious domain method that discretizes the ice and rock
 243 phases with Eulerian and Lagrangian approaches, respectively. The discretization pro-
 244 cess for each phase is independent of each other and does not require body-fitted meshes.
 245 As illustrated in Figure 2 (a), two sets of discretizations are used: The Lagrangian points
 246 are attached to and stay on the outline of bed shape Γ . In contrast, the Eulerian mesh
 247 spans the whole domain, Ω_i , including the area occupied by the solid structure.

248 The general idea of IBM is to solve the ice governing equation (1) and (9) on a Eu-
 249 lerian grid imposed on the ice domain, Ω_i , with a correction on the ice-bedrock inter-
 250 face Γ at each intermediate time step to impose the boundary condition. Here, we use
 251 the direct forcing implementation of IBM (Uhlmann, 2005). The implementation is de-
 252 composed into four steps. First, advance the governing equations (10) to (12) for one pseudo
 253 time step forward without considering the submerged bedrock. We refer to this solution
 254 as the intermediate fields $u^{n+1/2}$ and $T^{n+1/2}$

$$255 \frac{u_i^{n+1/2} - u_i^n}{\Delta\tau_u} = \left(\frac{\partial\tau_{ij}}{\partial x_j} \right)^n - \left(\frac{\partial p}{\partial x_i} \right)^n + F_i, \quad (14)$$

$$256 \frac{T_i^{n+1/2} - T_i^n}{\Delta\tau_T} = -\frac{\partial T}{\partial t} - \left(u_i \frac{\partial T}{\partial x_i} \right)^n + \frac{1}{\rho c_p} \left(\frac{\partial}{\partial x_i} \left(\kappa \frac{\partial T}{\partial x_i} \right) + 2\tau_E \dot{\epsilon}_E f(T - T_m) \right)^n, \quad (15)$$

257 where the superscript n represents the current pseudo time step and $\Delta\tau$ represents the
 258 pseudo time step size.

259 Second, we use a regularized delta δ function (Peskin, 2002) to translate the inter-
 260 mediate quantities $u^{n+1/2}, T^{n+1/2}$ from the Eulerian points x to that on the Lagrangian

261 points X_l . Dropping the superscript for simplicity, we have

$$262 \quad U(X_l) = \sum u(x)\delta(x - X_l)dxdz, \quad Q(X_l) = \sum q(x)\delta(x - X_l)dxdz, \quad (16)$$

263 where $q = \partial T / \partial x_i$ denotes the heat flux, dx and dz are the horizontal and vertical grid
 264 size, and the lower case and upper letters represent Eulerian and Lagrangian quantities,
 265 respectively. The delta function is a continuous differentiable function that takes 1 if the
 266 Eulerian grid point is on the Lagrangian point and 0 if far away, thus allowing a smooth
 267 transfer between the grids.

268 Third, we compute the volume forces F_U and F_Q required to achieve the desired
 269 boundary condition, in this case, the no-slip condition $U^d = 0$ and constant geother-
 270 mal heating condition Q^d

$$271 \quad \frac{U^{n+1/2} - U^d}{\Delta t} = F_U^{n+1/2}, \quad \frac{Q^{n+1/2} - Q^d}{\Delta t} = F_Q^{n+1/2}. \quad (17)$$

272 Finally, we use the computed volume force to correct the intermediate fields u and T and
 273 obtain the velocity and temperature fields at the next pseudo time step

$$274 \quad u^{n+1} = u^{n+1/2} + \frac{F_U^{n+1/2}}{\Delta V_{lag}}, \quad q^{n+1} = q^{n+1/2} + \frac{F_Q^{n+1/2}}{\Delta V_{lag}}, \quad (18)$$

275 where ΔV_{lag} is control volume of one Lagrangian points. In our model, we select the num-
 276 ber of Lagrangian points such that $\Delta V_{lag} \sim dxdz$.

277 The other interface that requires careful numerical treatment is the upper surface
 278 of the ice. Ice thins as it speeds up and the free surface moves downwards towards the
 279 bed. While the movement itself is relatively slow and gradual, its thermal implications
 280 could be very important (e.g., Mantelli et al., 2019). To capture ice thinning, we rep-
 281 resent the free surface as the level-set of a higher dimensional distance function, as il-
 282 lustrated in Figure 2 (b), allowing us to handle the moving front implicitly as discussed
 283 in the books by Sethian (1999) and Osher et al. (2004). More specifically, the ice-air in-
 284 terface is defined as the zero-contour of a signed distance function ϕ

$$285 \quad \phi(x) = \begin{cases} -d & \text{if } x \in \text{air}, \\ +d & \text{if } x \in \text{ice}. \\ 0 & \text{if } x \in \Gamma, \end{cases} \quad (19)$$

286 where d is the distance from the grid point to the interface. Across $\phi(x) = 0$, the den-
 287 sity ρ , viscosity η , and thermal conductivity κ change

$$288 \quad \rho(\phi) = \rho_a + (\rho_i - \rho_a)H(\phi), \quad (20)$$

$$289 \quad \eta(\phi) = \eta_a + (\eta_i - \eta_a)H(\phi), \quad (21)$$

$$290 \quad \kappa(\phi) = \kappa_a + (\kappa_i - \kappa_a)H(\phi), \quad (22)$$

291 where the subscript i denotes the material properties in the ice domain, subscript a de-
 292 notes those in the air domain, and H is the Heaviside function defined as

$$293 \quad H(\phi) = \begin{cases} 0 & \phi < -\epsilon, \\ \frac{1}{2} + \frac{\phi}{2\epsilon} + \frac{1}{2\pi} \sin \frac{\pi\phi}{\epsilon} & -\epsilon \leq \phi \leq \epsilon, \\ 1 & \phi > \epsilon, \end{cases} \quad (23)$$

294 with a smoothing length of $\epsilon = 3\Delta x$ (Sethian, 1999; Sethian & Smereka, 2003).

295 To evolve the location of the interface, we advect the level field using the general
 296 advection equation, also known as the level-set equation:

$$297 \quad \frac{\partial \phi}{\partial t} + u_n |\nabla \phi| = 0, \quad (24)$$

where u_n is the physical velocity in the normal direction of the ice surface. This equation moves the implicit front with the ice velocity field determined by the mechanical equation (1) at each physical time step. The spatial discretizations use first-order upwind, and the temporal discretizations use the second-order accurate Total Variation Diminishing Runge–Kutta schemes. Since the ice-air interface remains smooth at all times and thins only slightly as compared to the overall thickness of the ice sheet, sophisticated advection schemes such as extension velocities (Adalsteinsson & Sethian, 1999), topology-preservation techniques (Qin et al., 2015) or reinitialization (Osher et al., 2004) are not necessary in our case.

2.3 Verification

To verify the accuracy of our numerical method, we compare our numerical results to two analytical solutions: the circular inclusion test (Schmid & Podladchikov, 2003) and the classic Nye solution for the velocity field in ice flowing over a wavy surface (Nye, 1969). These two benchmarks are complementary, because the circular-inclusion test is better suited for identifying spurious oscillations in the pressure field while the Nye solution represents a flow configuration more closely related to the dynamic problem we aim to understand.

Following Schmid and Podladchikov (2003), we consider a circular solid inclusion immersed in a square domain with homogeneous fluid. We apply a pure shear boundary condition to the fluid domain and a no-slip to inclusion-fluid boundary. To evaluate the accuracy of the numerical scheme, we compare our numerical results to the analytical solutions of the pressure and velocity fields

$$v_x + iv_y = \epsilon R^2 \left(-\frac{1}{z} - \frac{z^3}{r^4} + R^2 \frac{z^3}{r^6} \right) + \dot{\epsilon} \frac{r^2}{z}, \quad (25)$$

$$P = 4\eta\epsilon \cos(2\theta) \frac{R^2}{r^2}, \quad (26)$$

where $z = x + iy = re^{i\theta}$, ϵ is the shear strain rate, η is the fluid viscosity and R is the radius of the inclusion. The boundary conditions applied are the pure shear strain rate

$$v_x = \dot{\epsilon}x, v_y = -\dot{\epsilon}y. \quad (27)$$

Figure 3 depicts the spatial convergences for the inclusion case, where (b) and (c) compare the results of numerical and analytical vertical velocity fields, (d) and (e) compare the results of pressure fields, and (a) shows that the combination of the Stokes solver and IBM leads to the spatial accuracy around order 1.5.

We further test our model with Nye’s analysis of the flow over wavy bed with a Newtonian fluid. We followed Nye (1969)’s model setting, and considered the bed shape in the form of a sine wave $z_0 = \epsilon a \sin(kx)$. The boundary condition is simple shear on the surface $(\tau_x, \tau_z) = (1, 0)$, periodic in the flow direction. Here, we limit our reference analytical solution to only first order $\mathcal{O}(\epsilon)$

$$u = U (1 + z\epsilon a\beta k^2 \exp(-kz) \sin(kx)) + \mathcal{O}(\epsilon^2), \quad (28)$$

$$v = U\epsilon a\beta k(1 + kz) \exp(-kz) \cos(kx) + \mathcal{O}(\epsilon^2), \quad (29)$$

$$p = 2\epsilon\eta U a\beta k^2 \exp(-kz) \cos(kx) + \mathcal{O}(\epsilon^2), \quad (30)$$

where U is the far field horizontal velocity, $\beta = k_*^2 / (k_*^2 + k^2)$, and k_* stands for the characteristic wavenumber of regelation. The full solution can be found in Nye (1969).

Figures 4 (b-c) show the comparison between the numerical and analytical vertical velocity fields. In (d), we show the pressure comparison along the $z = 2.2$ m horizontal line. It should be noted here that the analytical solutions we compare to is only to the first order. This is the reason for the observed slight discrepancies between the two solutions in the peak and low regions in panel (c). Panel (a) shows that the spatial accuracy of IBM and spatial solver together is around order of 1.5.

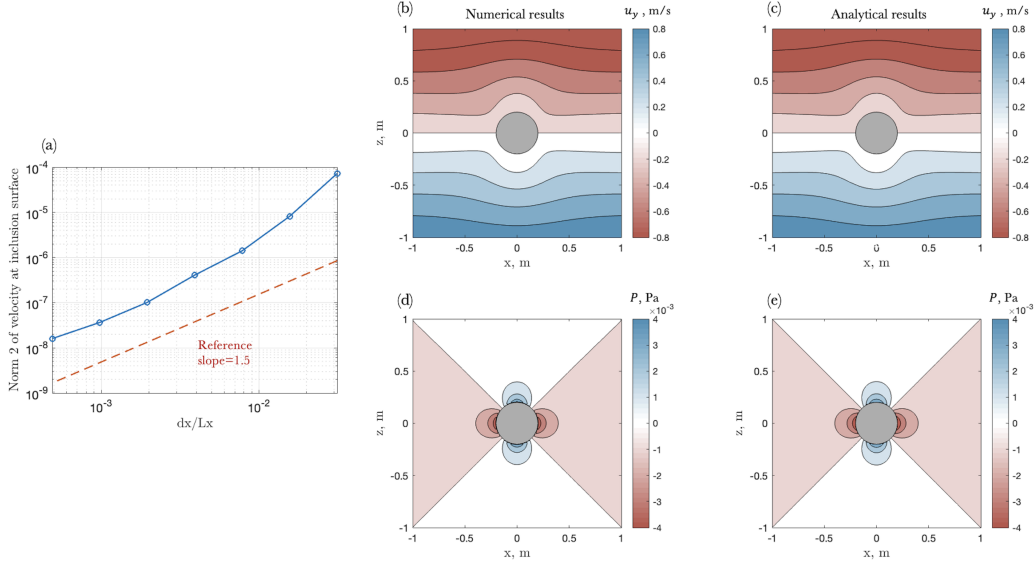


Figure 3. Spatial convergence test for the inclusion case . (a): L2 norm of the velocity at the cylinder. (b) and (c): Vertical velocity in the analytical case and numerical case, respectively. The black slid lines in (b) and (c) represent the streamlines. (d) and (e): Pressure in the analytical case and numerical case, respectively. The resolution shown here is 512 x 512.

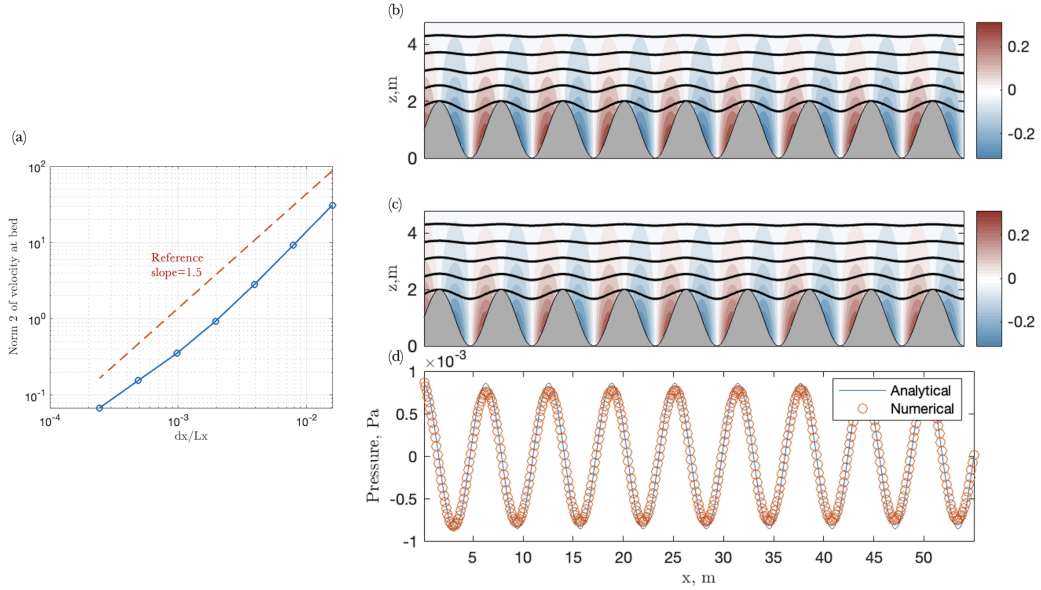


Figure 4. Comparison of numerical solutions against analytical solutions of Nye's problem (Nye, 1969). (a): L2 norm of the velocity at the bed. (b) and (c): Vertical velocity for the analytical and numerical case, respectively. The black slid lines in (b) and (c) represent the streamlines. (d): Pressure along the $z = 2.2$ m for both numerical and analytical cases. The resolution shown here is 512 x 128.

345 **3 Results**

346 We set our simulation domain size to 4800 m by 800 m across all simulations in this
 347 section. The surface temperature used in the simulations is prescribed as -26°C as a rep-

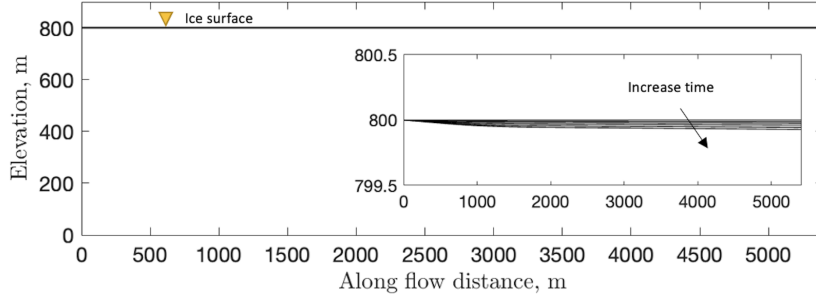


Figure 5. Ice surface evolution over 80 years on a flat bed. The sub-panel shows a zoom-in view of the ice surface evolution.

348 representative value for the surface temperature in Antarctica. Additionally, we apply a geother-
 349 mal heat flux of 0.05W/m^2 (Wright et al., 2012; Shapiro & Ritzwoller, 2004; Maule et
 350 al., 2005). The basal topography is modeled as $z_b = A \sin(kx)$, with an amplitude of
 351 $A = 100$ m and a wavenumber k ranging from 0.52 to 6.28.

352 For all simulations, we assume no-slip at the bed and a free surface. One example
 353 of the ice surface evolving over time is shown in Figure 5. At the scale of the model do-
 354 main, the ice-surface change is not immediately apparent, but a close-up view of the up-
 355 per tens of meters of the domain clarifies that the surface is evolving if only by a few me-
 356 ters or less than 1% of the ice thickness. Given this small change and our focus on shear
 357 localization near the bed, we only plot the bottom part of our model domain in the re-
 358 maining figures of this section.

359 3.1 Ice Flowing over Topography May Form an Internal Shear Band

360 To identify how basal topography affects internal deformation, we compare the thermo-
 361 mechanical deformation of ice flowing over an idealized sinusoidal topography to ice flow-
 362 ing without topographic control (Figure 6). All other parameters and boundary condi-
 363 tions are identical for the two cases. Here we use the the power-law rheology with the
 364 exponent $n = 3$ (Glen, 1952, 1955) and include water weakening in the effective vis-
 365 cosity as discussed in Section 2.1.

366 Figure 6 (a) shows the case of ice (light blue) flowing over a sinusoidal topography
 367 (dark grey) for the lower portion of our model domain. The ice speeds up from left to
 368 right as indicated by the green velocity profiles at four different along-flow locations of
 369 $x = 536, 1854, 3162, 4235$ m, where we compare the local velocity in dark green with
 370 inflow velocity in light green. This speed-up is facilitated by shear localizing $dudz$ in-
 371 creasingly on top of the topography as indicated in blue. The highest shear values oc-
 372 cur on the topographic highs, effectively linking these up into a continuous zone of el-
 373 evated shear strain rate. The control simulation of ice flowing over a flat topography is
 374 shown in Figure 6 (b). Similarly to Figure 6 (a), ice speeds up as it flows downstream,
 375 aided by shear strain rate in the immediate vicinity of the flat topography.

376 The main difference between the two simulations is how shear strain rate is distributed
 377 with depth (Figure 6, c). For the flat bed (Figure 6, b), the shear strain rate is highest
 378 nearest to the bed, whereas topography shifts the shear-rate maximum into the ice col-
 379 umn to a depth that is corresponds roughly to the height of the topographic peaks (Fig-
 380 ure 6, a). Both modes of deformation are capable of generating approximately compa-
 381 rable surface speeds of around 70 m/yr, with the ice flowing over rough topography mov-
 382 ing slightly faster at equal driving stress and basal resistance. Since the speed-up of the

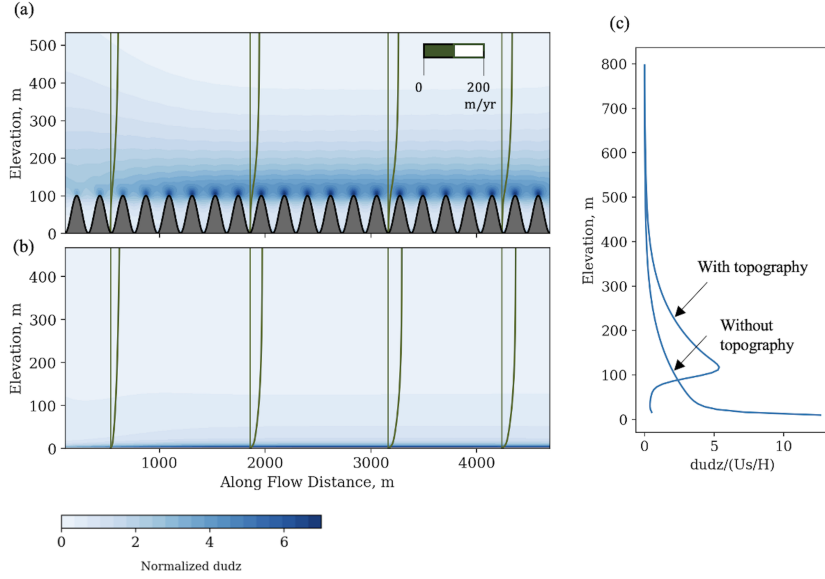


Figure 6. Role of basal topography in shear localization. (a) and (b): Shear strain rate $\partial u / \partial z$ in the background contour for the case of with basal topography and without basal topography. The velocity profiles at different locations along the flow are shown in the dark green lines, with a reference inflow velocity in light green lines. (c): Shear strain rate profile at $x = 4235$ m for both cases.

383 ice is gradual and not instantaneous, the cooling effect associated with ice thinning is
 384 not sufficient to prevent viscosity weakening in either of the simulations.

385 To quantify the share of total deformation accommodated within the ice as ice flows
 386 over the basal topography, we define \tilde{R}_d as the percentage of the internal deformation
 387 in the ice column to be the ratio of the integral of the shear strain rate from the bed up
 388 to some elevation z and the integral of the total shear strain rate in the entire ice col-
 389 umn

$$390 \quad \tilde{R}_d = \frac{\int_b^z \frac{\partial u}{\partial z}}{\int_b^s \frac{\partial u}{\partial z}} = \frac{u_z}{U_s}, \quad (31)$$

391 where subscripts d , b and s represent deformation, bed and surface, respectively. The
 392 tilde denotes a non-dimensional parameter. This parameter can also be interpreted as
 393 the velocity ratio: local x velocity divided by the surface x velocity in the same ice col-
 394 umn.

395 We use the term “shear band” to be a basal zone that accommodates the major-
 396 ity ($\geq 50\%$) of the total deformation in the ice column. We set the lower and upper bound
 397 of the internal shear band \tilde{R}_{dl} and \tilde{R}_{du} to 20% and 70%, respectively. Finally, we de-
 398 fine the bandwidth B_w as the vertical distance between these two bounds

$$399 \quad B_w = z(\tilde{R}_{du}) - z(\tilde{R}_{dl}). \quad (32)$$

400 Figure 7 shows how the shear band evolves within the model domain. Towards the left
 401 boundary, deformation is distributed relatively evenly as indicated by the 20% and 70%
 402 contour differing by several hundred meters in depth (Figure 7, a). As ice flows down-
 403 stream, the lower limit of the shear band, $\tilde{R}_{dl} = 20\%$, stays on top of the basal topog-
 404 raphy shape and does not change depth much. This result highlights that the depth-distribution
 405 of deformation below the topographic highs remains relatively unaffected by the shear
 406 localization and ice speeds up mainly at and above the topographic highs. The upper

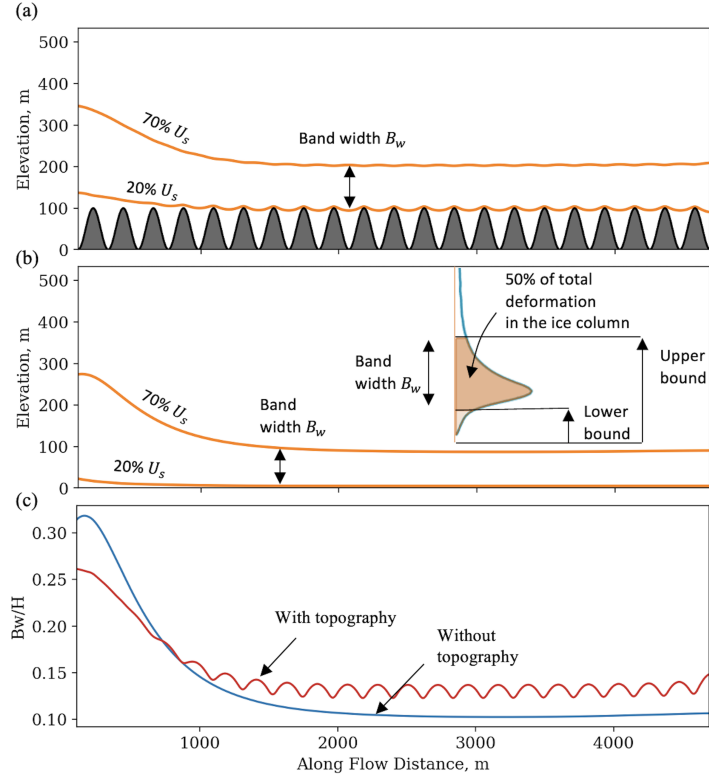


Figure 7. Shear band development along the flow. (a) and (b): Shear band development with and without a topography, defined as a basal zone where the 50% of total deformation in the ice column occurs. We define the lower and upper boundary of the shear band to be 20% and 70% of the deformation in the ice column, as illustrated in the sub-panel in (b). (c): Ratio of the shear band bandwidth B_w to the ice thickness H at that location along the flow for both cases.

407 limit $\tilde{R}_{du} = 70\%$ descends sharply, and then stabilizes around $z = 200$ m. For the case
 408 shown, the shear band has a width that is close to the amplitude of the sinusoidal bed
 409 shape, and accommodates approximately half of the total shear strain rate.

410 In the control case without topography, deformation also localizes due to viscos-
 411 ity weakening, but the shear band is located at the bed instead of within the ice column.
 412 The shear strain rate is maximal at the ice-bedrock interface with the $\tilde{R}_{du} = 20\%$ con-
 413 tour remaining very close to and almost at the bed (Figure 7, b). Figure 7 (c) shows the
 414 ratio of the shear band bandwidth B_w to the ice thickness H . Initially, the shear band
 415 width constitutes about 30% of the ice thickness for both cases. It decreases rapidly in
 416 the downstream direction, and finally stabilizes at a width of approximately 10% of the
 417 ice thickness.

418 **3.2 Shear Band Formation is The Consequence of a Positive Energy Bud-** 419 **get Near Topographic Peaks**

420 Similar to the creep instability, shear band formation is driven by the positive feed-
 421 back that localized deformation reduces ice viscosity that further localizes deformation.
 422 This feedback depends on the degree to which ice in the vicinity of topographic highs
 423 warms up during flow, as captured in the energy equation (9). Three terms contribute
 424 to the thermal evolution: advection, diffusion, and shear heating. Through a simple scal-

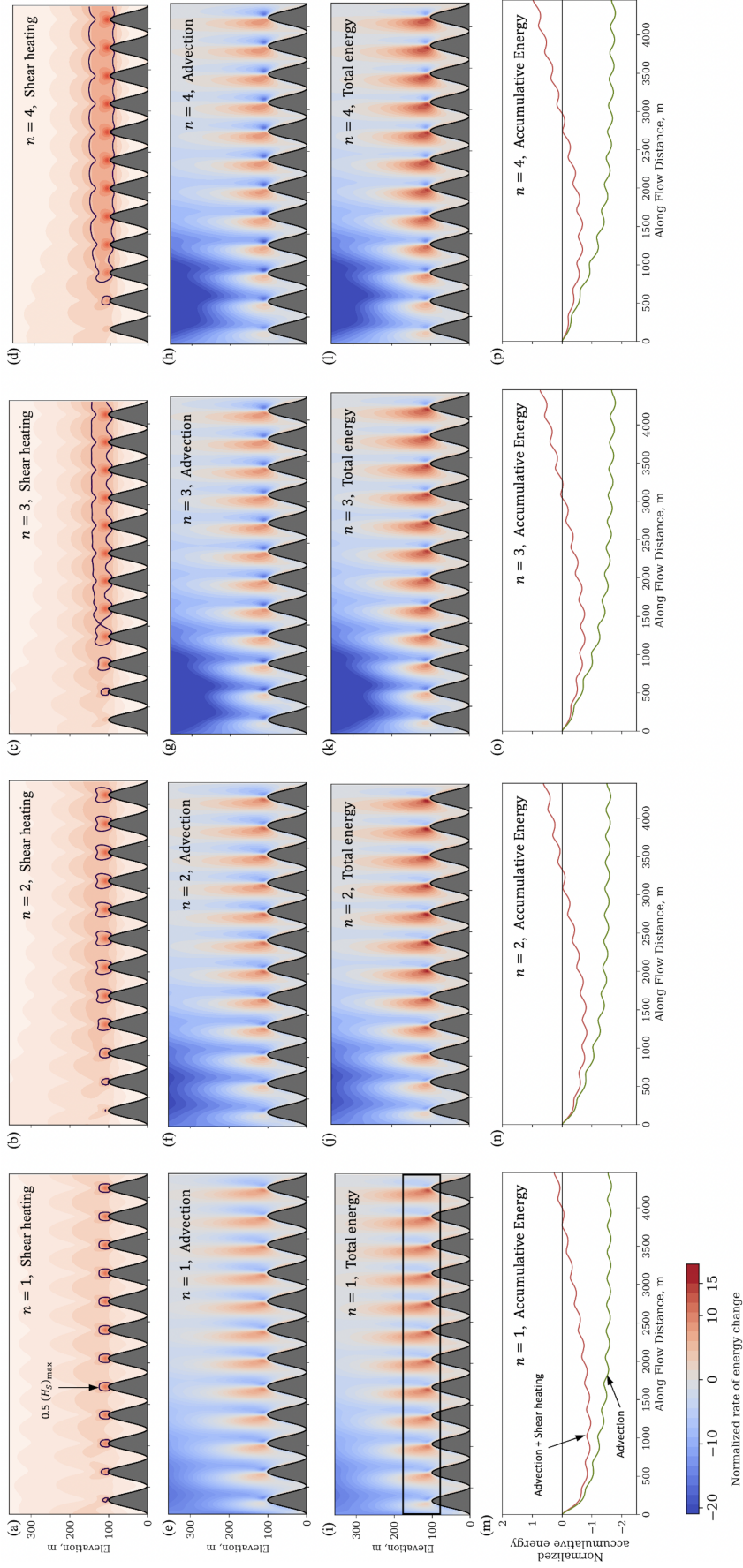


Figure 8. Role of the power-law exponent n on normalized shear heating \tilde{H}_s , vertical advection \tilde{A}_v , and approximated total energy \tilde{E} as defined in equation (33). First row (a-d): Normalized shear heating \tilde{H}_s contours in $x - z$ domain. The black contour lines denotes half of the maximum of \tilde{H}_s , in this case 3.15. Second row (e-h): Normalized vertical advection \tilde{A}_v contours. Third row (i-l): Normalized approximated total energy $\tilde{E} = \tilde{H}_s + \tilde{A}_v$ contours. Fourth row (m-p): Depth averaged accumulative total energy (red curves) and accumulative vertical advection (green curves) along x axis. The averaged area is indicated as the black box from $z = 80 - 180$ m in (i). Each column represents a different value of n as indicated in all panels. All simulations have the same basal topography of $Ak = 1.83$, where Ak is defined as the product of amplitude and wavenumber of the bed.

425 ing analysis (see Appendix A), we find that vertical advection and shear heating are the
 426 two primary competing terms in our case. In comparison, diffusion is roughly two or-
 427 ders of magnitude smaller than these two terms. Therefore, we approximate the total
 428 energy as the combined contributions of only vertical advection and shear heating.

429 To meaningfully compare the magnitude of advection and shear heating for differ-
 430 ent n from 1 to 4, we first divide the shear heating term $2\tau_E\dot{\epsilon}$ by ρc_p to ensure that both
 431 terms have the same units of K/s. We then normalize both terms using the character-
 432 istic shear heating $\rho g U_s \sin \alpha$, which represents the magnitude of shear heating at the
 433 bed, assuming that the x velocity varies linearly with depth. The non-dimensional ad-
 434 vection and shear heating terms can be then expressed as

$$435 \quad \tilde{H}_s = \frac{2\tau_E\dot{\epsilon}}{\rho g U_s \sin \alpha}, \quad \tilde{A}_v = \frac{\partial T}{\partial z} \frac{u_z c_p}{g U_s \sin \alpha}, \quad (33)$$

436 where H_s is shear heating, A_v is vertical advection, U_s is the surface speed, u_z is the ver-
 437 tical velocity, and tilde represent non-dimensional quantities. Figure 8 compares the rate
 438 of normalized energy change attributed only to shear heating (first row), vertical advec-
 439 tion (second row), and the approximated total energy (third row) for values of n rang-
 440 ing from 1 to 4 (column 1 to 4). We plot the energy change over time on the same color
 441 scale for the first three rows for easier comparison.

442 In Figures 8 (a-d), the black contour lines highlight half of the maximum shear heat-
 443 ing value ($\tilde{H}_s = 3.15$). The heating is positive throughout the domain and concentrates
 444 within the internal shear band extending on top of topographic highs. The rate of heat-
 445 ing tends to increase in the downstream direction. Notably, for $n = 1$, shear heating
 446 on topographic highs is minimal. As the value of n increases, these localized shear heat-
 447 ing regions begin to connect and form a band situated above the topography. For ex-
 448 ample, in Figure 8, zones of elevated shear heating begin to bridge when $n \geq 3$.

449 The primary effect of vertical advection is cooling (Figures 8, e-h). Particularly in
 450 the left third of the domain where cold ice is drawn down from the surface. This cool-
 451 ing effect is also reflected in the dipping of the iso-velocity-ratio lines in Figures C1 and
 452 C2. In the immediate vicinity of topographic highs, however, vertical advection is posi-
 453 tive in the windward side of the obstacle and negative on the lee side, as evidenced by
 454 the alternating blue and red regions.

455 Summing shear heating and vertical advection produces the approximate total en-
 456 ergy, indicative of the energy budget of the basal ice (Figures 8, i-l). The impact of shear
 457 heating is primarily confined to the vicinity of the basal topography, as deformation is
 458 predominantly concentrated near the bed. However, upon closer examination, it becomes
 459 evident that the lee side of the bumps, characterized by negative advection, is partially
 460 balanced by shear heating. The windward side of the bumps, dominated by positive ad-
 461 vection, experiences reinforcement.

462 We calculate the depth-averaged accumulative quantities for total energy and ver-
 463 tical advection within the specified range from z_1 to z_2 , as indicated by the black box
 464 in (i)

$$465 \quad \overline{\tilde{H}_s}(x) = \int_0^x \frac{1}{z_2 - z_1} \int_{z_1}^{z_2} \tilde{H}_s dz dx, \quad \overline{\tilde{A}_v}(x) = \int_0^x \frac{1}{z_2 - z_1} \int_{z_1}^{z_2} \tilde{A}_v dz dx. \quad (34)$$

466 This cumulative measure serves as an indicator of the energy carried by the ice as it flows
 467 downstream. To focus on the basal region of interest, we select a depth-averaged range
 468 of 80-180 m, setting the interval to align with the amplitude of the sinusoidal bed.

469 Figures 8 (m-p) depict the cumulative energy profiles, where the green curves rep-
 470 resent $\overline{\tilde{A}_v}$, considering only vertical advection, and the red curves represent $\overline{\tilde{E}}$, consid-
 471 ering both vertical advection and shear heating. $\overline{\tilde{A}_v}$ consistently exhibits negative val-
 472 ues for all values of n , indicating that the ice within the basal region does not experi-

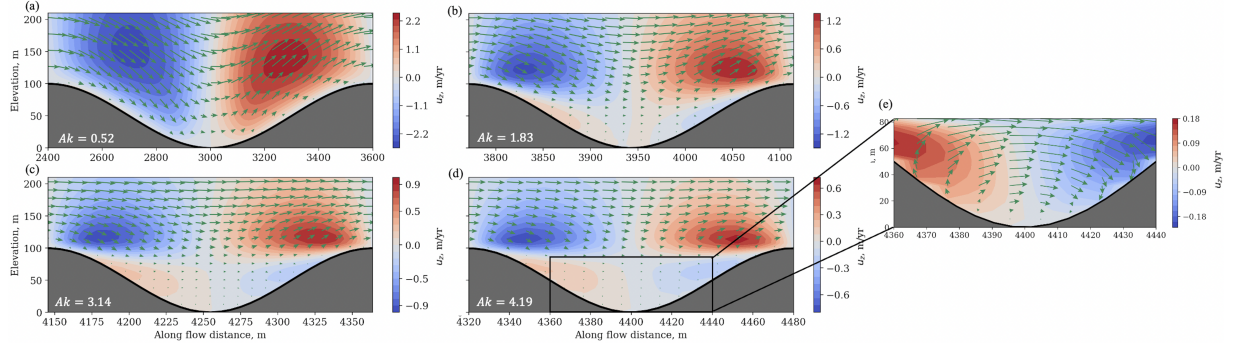


Figure 9. Role of basal topography shape in flow separation for $n = 3$. Each panel presents the vertical velocity contours and velocity vectors corresponding to a specific value of Ak , namely 0.52 (a), 1.83 (b), 3.14 (c), and 4.19 (d). (e) shows a zoomed-in perspective of the bottom of trough of (d).

473 ence positive energy gain. However, upon incorporating shear heating alongside verti-
 474 cal advection, \overline{E} gradually becomes positive in the downstream direction. This trend holds
 475 true across all values of n , although higher values of n tend to amplify the extent of cumu-
 476 lative total energy.

477 One important implication of shear band formation as shown in Figures 8 (e-h) is
 478 a separation of the flow in the ice: The ice above the shear-band moves relatively fast
 479 and is characterized by a simple flow field dominated by speed-up in the flow direction.
 480 In contrast, basal ice slows down as the shear band accommodates the majority of the
 481 deformation. The flow field in the basal ice underneath the shear band is more complex.
 482 Figure 9 shows how the degree of flow separation varies for four different topographies
 483 defined by the shape factor Ak that represents the product of amplitude and wavelength
 484 of the bed. We show the flow field only for a single trough with shape factors Ak of 0.52,
 485 1.83, 3.14, and 4.19 for a rheological power-law exponent of $n = 3$.

486 For a relatively low value of Ak (Figure 9, a), ice follows the downhill and uphill
 487 contours of the topography, maintaining a smooth flow. As Ak increases to 1.83 (Fig-
 488 ure 9, b), at the bottom of the trough there is a slight upward flow near the bed on the
 489 downhill side and a downward flow on the uphill side, indicating the onset of separation.
 490 As Ak continues to rise (Figures 9, c-e), this trend becomes more pronounced. Between
 491 the bumps, four distinct regions emerge: Above the peak of topography, the flow still
 492 exhibits the characteristic down-up motion. Below the peak, the flow in the trough re-
 493 verses its direction, moving back from the uphill side of the next bump to the downhill
 494 side of the previous bump (Figure 9, e).

495 The separation line, which marks the division of flow, is positioned slightly
 496 below the peak of the topography. In the case of $A = 100$ m, the separation line is approx-
 497 imately located at $z = 80$ m. The occurrence of flow separation is important because
 498 it leads to a division of the flow in the vertical direction. The presence of flow separa-
 499 tion could hence be an indicator for the existence of an internal shear band. The lower
 500 portion experiences relatively slow, re-circulatory motion ($u < \sim 0.2$ m/yr). In contrast,
 501 the upper portion flows over a bed that “appears smoother” than its actual shape. Con-
 502 sequently, when flow separation occurs, the ice situated above the basal topography may
 503 not feel the complete underlying bed shape.

504 **3.3 Scaling of Internal Shear Band Formation Using Topography and** 505 **Rheology parameters**

506 In Sections 3.1 and 3.2, we found that shear heating can dominate over advection
 507 near topographic peaks, leading to a net increase in energy budget in basal ice. The in-
 508 ternal shear band development depends not only on power-law-exponent n , but also on
 509 the shape of the sinusoidal topography Ak . In this section, we aim to understand the
 510 dual effect of these two parameters and quantify their role in inducing shear localization
 511 through scaling analysis and numerical simulations.

512 For our scaling analysis, we consider a steady state internal shear band under a spe-
 513 cific sinusoidal shape characterized by Ak and rheology exponent n . We assume that the
 514 ice flow is fully developed in x direction, thus all $\partial/\partial x$ becomes zero. The momentum
 515 equation in x direction can then be simplified to

$$516 \quad \frac{\partial(\eta\epsilon_{xx})}{\partial x} + \frac{\partial(\eta\epsilon_{xz})}{\partial z} = -\rho g \sin \alpha. \quad (35)$$

517 We impose a generic power-law rheology without temperature dependence and assume
 518 the main stress component is the shear stress, i.e., $\tau_E \approx \tau_{xz}$. The viscosity has the fol-
 519 lowing form

$$520 \quad \eta = \frac{1}{2} a_0^{-\frac{1}{n}} \left(\frac{\partial u}{\partial z} \right)^{-1 + \frac{1}{n}}. \quad (36)$$

521 For the sinusoidal topography, we choose the characteristic horizontal length l to be \sim
 522 $\lambda^{(n-1)p} A^{1-(n-1)p}$, where p is some constant and n is the power-law exponent. We choose
 523 this the exponent such that the characteristic horizontal length scale have the same unit
 524 as length, and we choose $(n-1)$ to avoid zero denominator in the later derivation. Af-
 525 ter substituting all of these into the momentum equation and with the relationship $Ak =$
 526 $2\pi A/\lambda$, we have

$$527 \quad B_w \propto (Ak)^{-2pn}. \quad (37)$$

528 For a more detailed derivation, please refer to Appendix B.

529 To test the derived scaling relationship against our simulations, we conduct four
 530 sets of numerical experiments with $n = 1, 2, 3, 4$. We include a range of shape factor
 531 Ak values spanning from 0.52 to 6.28. Shape factor $Ak = 0.52$ corresponds to wave-
 532 length is 16 times larger than amplitude, and $Ak = 6.28$ corresponds to the scenario
 533 where the amplitude of the bump matches the wavelength. Figure 10 shows $dudz$ vari-
 534 ations with different exponent n and shape factor Ak . Here, we normalize the absolute
 535 value $dudz$ by U_s/H where U_s is the surface speed and H is the ice thickness for bet-
 536 ter comparison across different Ak and n .

537 The influence of Ak on shear localization and shear band forming is similar across
 538 all n . When Ak is low (Figures 10, a-d), shear deformation $dudz$ is concentrated around
 539 the topographic peaks. As Ak increases, $dudz$ localization on the peaks begins to con-
 540 nect and bridges as anticipated, e.g. Figures 10 (c,g,k). When Ak is approximately 2 or
 541 larger, the shape of the 70% U_s and 20% U_s contour lines, depicted in solid orange lines
 542 in all panels, become less wiggly and no longer align with the underlying shape of the
 543 basal topography (Figures 10, j-l). Accordingly, the bandwidth stabilizes with fewer os-
 544 cillations (Figures 10, n-p).

545 The relationship between B_w/H , Ak and n is depicted in Figure 11. Each marker
 546 represents a normalized bandwidth value corresponding to a specific shape factor and
 547 exponent from the simulations. To determine the stabilized bandwidth, we compute the
 548 average bandwidth value across three consecutive bumps in the downstream region of
 549 the domain. We exclude the upstream part from the averaging process due to the on-
 550 going rapid thinning of the ice, which could lead to an overestimation of the bandwidth.

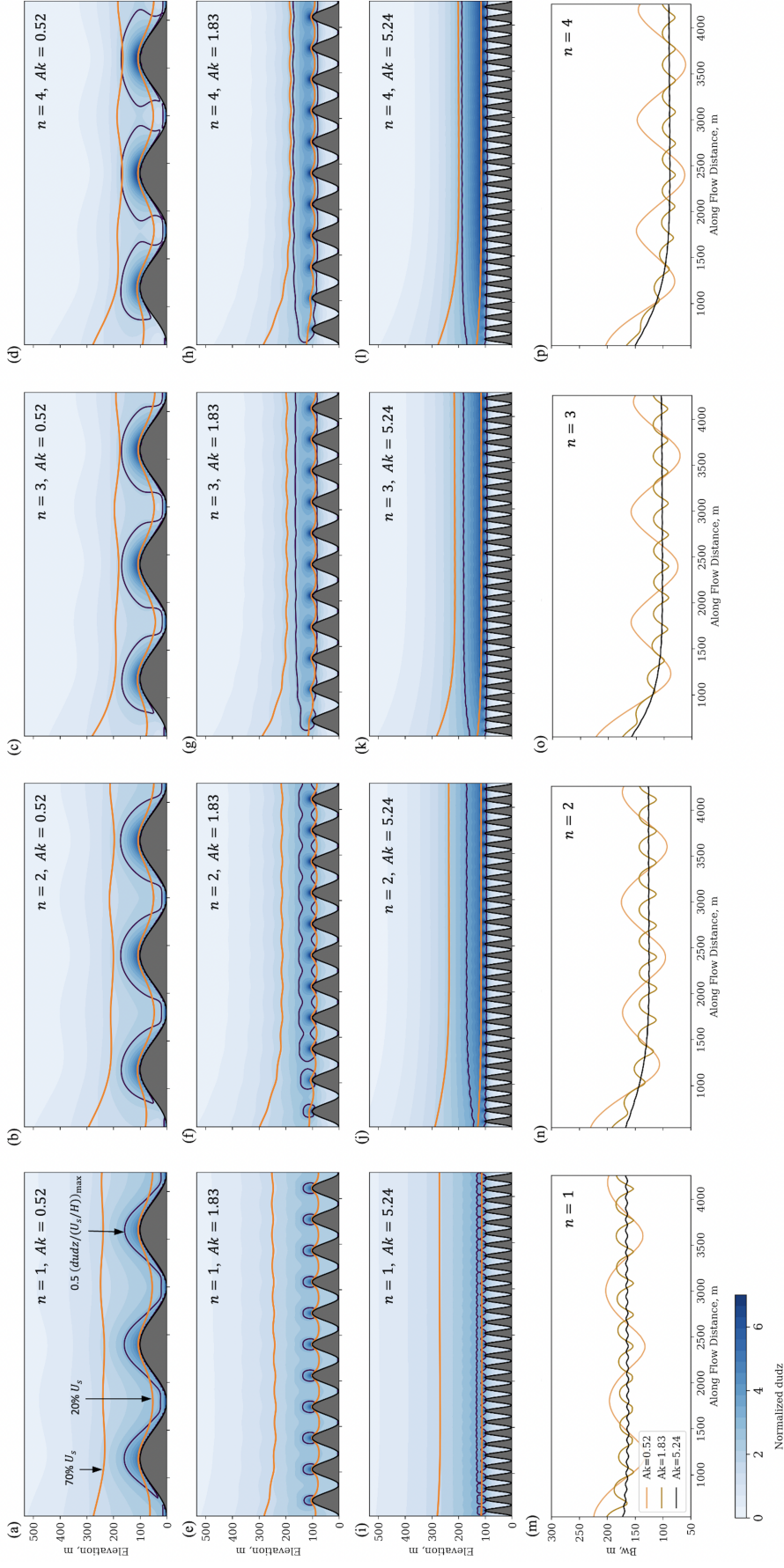


Figure 10. The normalized deformation $dudz$ variations with different exponent n and shape factor Ak . The first three rows corresponds to shape factors $Ak = 0.52$ (a-d), 1.83 (e-h), and 5.24 (i-l), respectively. Each column represents a specific value of the exponent n . In the first three rows of each panel, the two orange lines indicate the contours of 70% U_s and 20% U_s as defined in equation (31) and illustrated in Figure 7. The black contour in the first 3 rows in each panel highlights half of the maximum value of $dudz/(U_s/H)$, in this case 3.15. The last row (m-p) show how the thickness of the bandwidth, defined as the vertical distance between 70% U_s and 20% U_s lines, varies along the flow for different shape factors and exponents.

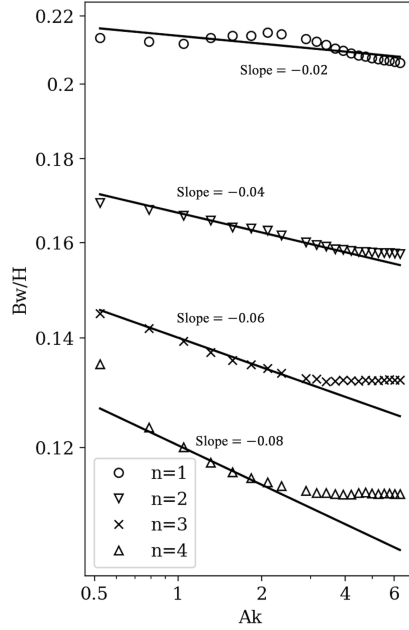


Figure 11. The regime diagram of the internal shear bandwidth B_w/H , power-law exponent n , and shape factor Ak of the sinusoidal bed. Each marker shape corresponds to a distinct simulation set sharing the same n value, and each individual marker represents a single simulation.

551 In cases where the Ak value is too small to achieve three consecutive stable bumps, we
 552 adjust the number of averaged bumps accordingly. The selection of the averaging area
 553 is outlined in Figures C1 and C2.

554 Observing the gradual increase in Ak , we note a corresponding decrease trend in
 555 the width of the internal shear band for all n . The rate of this decrease varies, with a
 556 slope of the logscaled relationship approximately following a pattern of $-0.02n$. This sug-
 557 gests that for larger values of n , the width of the shear band reduce at a faster rate, thus
 558 localizing the deformation significantly more. It is evident that when Ak continues to
 559 increase, the averaged bandwidth eventually stabilizes around a certain value (Figure
 560 11 down-triangle, cross, and up-triangle markers). This critical Ak value at which the
 561 width stabilizes decreases as n increases. Specifically, we observe that the widths sta-
 562 bilize around $Ak = 4.45, 3.14, 2.62$ for $n = 2, 3, 4$ respectively. However, this trend
 563 is less pronounced for $n = 1$. Even at the most rugged topography considered, where
 564 the amplitude equals the wavelength, a stable width of the shear band is still not observed
 565 (Figure 11 circle markers).

566 By varying the basal topography shape factor Ak and exponent n , we can conclude
 567 from the numerical experiments that for each exponent n , there exist a steady state shear
 568 band width as $Ak \rightarrow \infty$ (Figure 11). When Ak is high, the velocity ratio contours tend
 569 to concentrate at a consistent elevation and do not align with the shape of the basal top-
 570 ography (Figures C1 and C2). This suggests that the perturbations originating from
 571 the basal topography propagate upwards from the bed to the surface only over distances
 572 spanning tens to a few hundred meters, depending on the value of n . Thus, the influ-
 573 ence of the actual basal topography shape on the internal ice above this level is likely
 574 reduced, and the internal ice progressively “perceives less” of the specific shapes of the
 575 basal topography.

576 The scaling relationship between the bandwidth and non-dimensional shape factor
 577 Ak raised to the power of $-2pn$ is shown as the solid lines in Figure 11. From the
 578 simulation results, we infer that the value of p takes around 0.01. Before the width of
 579 the shear band stabilizes, the scaling of $-2pn$ captures the decreasing rate very well. Yet
 580 it is important to acknowledge that this scaling relationship does not account for the in-
 581 fluence of temperature-dependent rheology and flow variations in the x direction (i.e.,
 582 assume fully developed flow). Consequently, the aforementioned relationship tends to
 583 slightly underestimate the actual degree of localization.

584 As the spacing between two bumps approaches infinitesimally small values ($Ak \rightarrow$
 585 ∞), scaling suggests B_w tends towards zero, which is physically unrealistic. A zero thick-
 586 ness for the internal shear band implies the presence of internal “slip” where velocity be-
 587 comes discontinuous. Since our model focuses on understanding flow localization, it does
 588 not permit a discontinuities in velocity anywhere in the computational domain. Hence,
 589 as $Ak \rightarrow \infty$, we anticipate that B_w will stabilize after surpassing a specific Ak value,
 590 indicating that the thickness of the internal shear band has reached its minimum pos-
 591 sible value for a given n .

592 4 Discussion

593 The fast speed of many glaciers and ice streams are thought to be accommodated
 594 by basal sliding with internal deformation contributing only minimally (Echelmeyer &
 595 Zhongxiang, 1987; Hermann & Barclay, 1998; Rignot et al., 2011; Rignot & Mouginot,
 596 2012). However, recent advances in our understanding of the different deformational regime
 597 of ice particularly at high stresses (Goldsby & Kohlstedt, 2001), a growing appreciation
 598 for the sharp weakening of ice near pre-melting conditions (Krabbendam, 2016), and field
 599 evidence of complex, depth-dependent deformation in fast-moving ice (Law et al., 2023;
 600 Maier et al., 2019; Hills et al., 2017) merit a re-evaluation of the degree to which inter-
 601 nal deformation may contribute to fast ice motion.

602 In the presence of complex basal topography, internal deformation may actually
 603 have more localization than usually expected when most glacier models tend to use a
 604 smooth bed due to the bed resolution limitation (Law et al., 2023). While Law et al. (2023)
 605 focuses more on descriptive aspects of ice motion at specific field sites, our study com-
 606 plements the finding of spatially variable deformation along depth by bringing in an in-
 607 depth analysis of two physical processes that contribute to this spontaneously formed
 608 localization: vertical advection and shear heating. We show that vertical advection is
 609 proportional to the rate of thinning and therefore the rate of glacier acceleration. When
 610 shear heating dominates over the vertical advection, the net energy gain in the shear band
 611 region becomes positive and provides a necessary condition for an internal shear band
 612 to form. Otherwise, when net energy gain is negative or oscillates around a very small
 613 value, and shear band formation is suppressed. The accumulative approximated total
 614 energy, defined as the sum of shear heating and vertical advection, grows with increas-
 615 ing nonlinearity in ice rheology, captured by the power-law exponent n , for a given to-
 616 pography.

617 Basal topography amplifies shear heating, because it causes additional deformation
 618 within the ice. Importantly, this deformation is not reduced but instead amplified
 619 by speed-up as ice is forced to wrap around topographic highs at increasing speed. We
 620 emphasize that the high-degree of shear localization occurring within an internal shear
 621 band does not represent sliding. In our simulations, ice is frozen to the bed while an in-
 622 ternal shear band forms above it, creating flow separation between the slow-moving ice
 623 trapped in topographic troughs and the fast-moving ice above the internal shear band.
 624 As speed-up continues, it is possible that the ice underneath the internal shear band grad-
 625 ually warms and becomes temperate. The existence of temperate zones with variable ver-

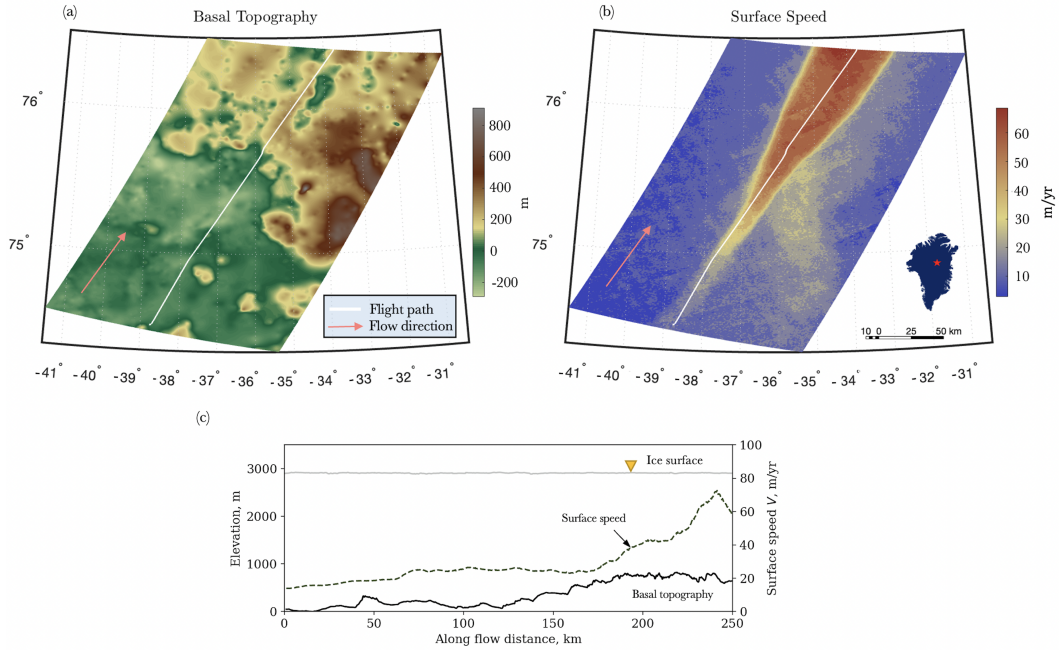


Figure 12. Basal topography and surface speed at NEGIS. (a): basal topography contour from BedMachine 3 (Morlighem et al., 2017). (b): surface speed contour from MEaSUREs NSIDC (Joughin et al., 2015). (c): surface speed (dashed line) change with the basal topography (black solid line) along flight path, indicated as the white lines in (a) and (b). The ice surface is shown as a grey solid line. The basal topography and ice thickness in (c) is obtained from Franke et al. (2021).

626 tical extent depending on topography is supported by borehole data (Harrington et al.,
 627 2015; Hills et al., 2017; Law et al., 2023).

628 Our simulations demonstrate that the speed-up associated with the formation of
 629 an internal shear band is gradual in the sense that it develops over spatial scales larger
 630 than the ice-thickness. In field settings where an increase in ice surface speed appears
 631 to correlate with a change in basal roughness, speed-up tends to occur on a similar scale
 632 of multiple ice thickness, such as the Northeast Greenland Ice Stream (NEGIS) (Bamber
 633 et al., 2001), the Siple Coast Ice Streams (Siegert et al., 2004), and the Institute Ice Stream
 634 (Bingham & Siegert, 2007). For example, Figure 12 shows that the basal topography at
 635 NEGIS becomes more pronounced in the flow direction (Figure 12, a) and that the surface
 636 speed increases as the ice stream broadens (Figure 12, b).

637 We show the NEGIS example here merely to demonstrate that the type of dynamics
 638 identifies in our idealized simulations could have ramifications for understanding ice
 639 dynamics in specific field settings. It is an interesting example for shedding light on the
 640 relevant scales contributing to ice speed-up: The spatial scale over which topographic
 641 peaks vary prior to 170 km downstream is tens of meters (Figure 12, a). This scale is
 642 small as compared to the ice thickness of several hundred meters, but larger than the
 643 small-scale roughness of a few meters considered in existing sliding laws (e.g., Weertman,
 644 1957; Nye, 1959; Liboutry, 1968; Fowler, 2010; Schoof, 2005; Bindschadler, 2006; Petrat
 645 et al., 2012). As a consequence, these intermediate scales are challenging to capture in
 646 large ice-sheet models. One contribution of our work is to advance our understanding
 647 and ability to capture the ice-dynamics implications of these intermediate-scale topo-
 648 graphic variations in ice-sheet models, for example by smearing out the transition from

649 flow-to-sliding over this scale (Bueler, 2009). Figure 12 exemplifies an interesting cor-
 650 relation between basal topography and surface speed, but it would be challenging to our
 651 model results against this data alone, because it does not constrain the potentially com-
 652 plex, depth-dependence of deformation within the ice.

653 A more direct comparison are borehole measurements of ice properties with depth.
 654 For example, Maier et al. (2019) drilled a network of eight boreholes at a slowly mov-
 655 ing ridge located 33 km from the terminus of Issunguata Sermia within the ablation zone
 656 of the western margin of the Greenland Ice Sheet. Their measurements show a high shear
 657 strain rate concentrated within around 10 – 50 m above the bedrock, but nearly zero
 658 shear strain rate is observed at bedrock. Such a high localization of shear strain rate in
 659 the interior of the ice evinces the possibility of internal sliding interface. The data in-
 660 dicates a pronounced increase in shear strain rate at an elevation of tens of meters above
 661 the bed followed by a rapid decrease in shear strain rate in the immediate vicinity of the
 662 bed. In Figure 13 (b), we use our model to match the height where rapid decrease of shear
 663 strain rate occurs in the borehole data ($A = 5.5$ m) and a typical Greenland atmospheric
 664 temperature ($T_s = -12^\circ\text{C}$). Figure 13 (c) shows the vertical strain rate profile for a con-
 665 trol run without basal topography. Only Figure 13 (b) is able to exhibit the observed
 666 drop in shear strain rate near the bed.

667 An important disconnect between Figures 13 (a) and (b-c) is the magnitude of the
 668 shear strain rate. Both of our model results show a shear strain rate that is about an
 669 order of magnitude higher than observed value in order to match the surface velocity of
 670 approximately 70 m/yr. Figures 13 (d-f) show the velocity profile with depth as inferred
 671 by Maier et al. (2019) from measurements (d), obtained from our simulations with basal
 672 topography (e), and without (f). Together, the panels demonstrate that our current model
 673 setup can either match the surface speed or the measured strain rates, but not both. The
 674 most likely explanation for this disconnect is that the observed surface speed is largely
 675 facilitated by basal sliding as sketched in Figure 13 (d), while the peak in shear strain
 676 rate may constitute the remnant of an internal shear band that may formed upstream
 677 when ice was still flowing over a topographicly variable bed.

678 In addition to borehole measurements of shear strain rate, our model could have
 679 important implication for depth-variability of ice fabric. For example, borehole data of
 680 grain size and cone angles collected at Siple Dome Antarctica by DiPrinzio et al. (2005)
 681 and reanalyzed by Pettit et al. (2011) reveals a localized band of small ice crystals and
 682 highly oriented fabric, located several hundred meters above the bed. Several processes
 683 could contribute to the development of this ice fabric with stress being a prominent fac-
 684 tor, as supported by strain rate data. However, the observed shift in fabric occurs around
 685 the depth of the Holocene transition, highlighting that climate history may also play a
 686 role (Pettit et al., 2011). Despite its age, this ice fabric continues to control ice flow by
 687 partially decoupling of the flow field above and below the shear band. The flow field be-
 688 comes three-dimensional, potentially to the degree of eddies forming (Meyer & Creyts,
 689 2017).

690 We emphasize that our model only considers a simplified, hard-rock basal topog-
 691 raphy. In reality, subglacial beds are significantly more complex and dynamic. For ex-
 692 ample, a sharper topography is capable of generating more localization compared to a
 693 smooth sinusoidal shape. Nonetheless, the development of an internal shear band would
 694 still rely on similar physical processes, most importantly a positive accumulative energy
 695 gain.

696 The presence of tills or other sediments underneath the ice introduces further com-
 697 plexity, both from a dynamic and from a mechanical point of view (e.g., MacAyeal, 1989;
 698 King et al., 2009; Hoffman & Price, 2014; Minchew & Meyer, 2020) and a thermal point
 699 of view (e.g., Rempel, 2008; Christoffersen & Tulaczyk, 2003). One potentially interest-
 700 ing implication of the flow separation we are identifying is that basal ice might interact

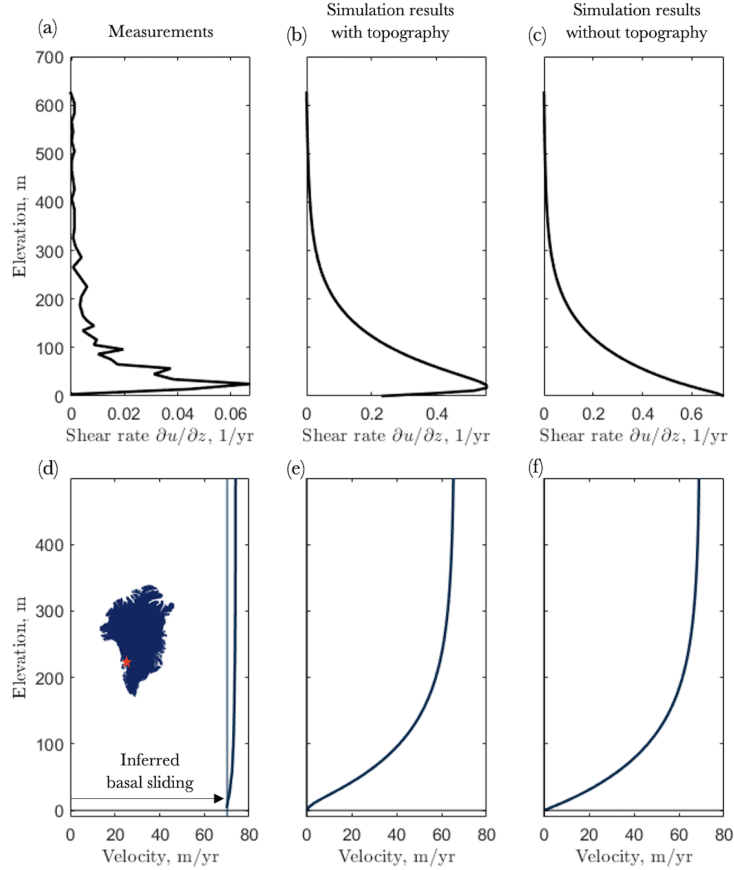


Figure 13. Comparison of model results to field measurements. The first column (a,d) shows the measurements at West Margin Greenland (Maier et al., 2019). Second (b,e) and third (c,f) columns show the simulation results with and without topography, respectively. The first row (a-c) shows the shear strain rates $\partial u/\partial z$ distribution in the depth direction. The second row (d-f) show the corresponding velocity profile for each case. In (d), the velocity profile is inferred by integrating the shear strain rate $\partial u/\partial z$ in (a) assuming there is basal sliding (Maier et al., 2019). Both simulations use the power-law rheology with exponent $n = 3$. The domain extend is set as 4800 m by 650 m. Bed height is set as 5.5 m and surface temperature is set as -12°C . In the second and third columns, the shear strain rates and velocity profiles are obtained at $x = 4235$ m.

701 in at least two distinct ways with a soft bed. One possibility is that fast ice motion and
 702 intense shear localization could lead to warm basal ice, generating interstitial water that
 703 drains to the bed. A thick layer of temperate can then form in topographical lows (Law
 704 et al., 2023) and create basal melt (Karlsson et al., 2021). Alternatively, basal ice in troughs
 705 may slow down because the shear band above it accommodates most of the deformation
 706 and cool down, potentially to the degree that underlying sediments freeze into the ice,
 707 as observed by Andreassen and Winsborrow (2009).

708 An important limitation of our study is the assumption of a two-dimensional model
 709 along the centerline (x, z) plane of an ice stream. This assumption neglects any varia-
 710 tions in the transverse y direction, both in the ice flow and the shape of the basal topog-
 711 raphy. In reality, the transverse inflow could have a significant impact on temperature
 712 and hence shear band formation. Near the shear margin, for instance, the presence of
 713 cold ice supplied from ice ridges leads to advective cooling, which counteracts viscous

714 heating effects (Suckale et al., 2014; Meyer & Minchew, 2018; Hunter et al., 2021; Schoof
715 & Mantelli, 2021). Basal topography is also three-dimensional, allowing the ice not only
716 to move up and down of obstacles but also to flow around them. This lateral motion can
717 mitigate some of the concentration of deformation that would occur exclusively at the
718 peaks of the topography in the two-dimensional case we consider.

719 5 Conclusion

720 This study aims to investigate the influence of basal topography on the formation
721 of internal shear band in ice flows using a thermo-mechanical Stokes flow model. By in-
722 corporating sinusoidal basal topography and comparing it with a flat topography control
723 case, we observe extensive shear localization on topographic highs, resulting in the
724 development of internal shear band. We analyze the impact of a power-law rheology with
725 different exponents $n = 1, 2, 3, 4$ and find that non-linear rheology enhances shear heat-
726 ing, tilting the energy balance towards heating in the basal region of the ice. Moreover,
727 we discover that the width of the internal shear band scales with the shape factor Ak
728 raised to the power of $-2pn$, indicating that the development of the shear band is in-
729 fluenced by the topography shape. Specifically, higher values of Ak facilitate the con-
730 nection and bridging of shear heating and shear deformation localization, increasing the
731 likelihood of internal shear band formation. These findings contribute to the understand-
732 ing of ice-sheet dynamics and provide insights for incorporating the spatial scale of the
733 flow-to-sliding transition into ice-sheet models, such as Bueler (2009).

734 6 Open Research

735 The current version of the numerical thermo-mechanical model with a build-in non-
736 linear rheology model is available from DOI repository (Zenodo) at: [https://doi.org/
737 10.5281/zenodo.7392224](https://doi.org/10.5281/zenodo.7392224). This model is developed based on the FastICE that can be
738 found at: <https://doi.org/10.5281/zenodo.3461171> (Räss et al., 2020). The bore-
739 hole data of shear deformation in Figure 13 (a) to compare against simulation results
740 can be found from Maier et al. (2019). The basal topography data in Figure 12 (a) can
741 be found at: <https://nsidc.org/data/idbmg4/versions/5> (Morlighem et al., 2017).
742 The ice surface speed data in Figure 12 (b) can be found at: [10.5067/MEASURES/CRYOSPHERE/
743 nsidc-0478.001](https://doi.org/10.5067/MEASURES/CRYOSPHERE/nsidc-0478.001) (Joughin et al., 2015). The basal topography data in Figure 12 (c) can
744 be found at: <https://doi.pangaea.de/10.1594/PANGAEA.907918> (Franke et al., 2021).

745 Acknowledgments

746 This work was supported by the NSF CAREER grant # 2142651. We acknowledge help-
747 ful conversations about this work with Paul Summers, Daniel Martin, Dustin Schroeder,
748 Eric Dunham, and Elisa Mantelli. We also appreciate the constructive inputs from As-
749 sociate Editor Olga Sergienko and two anonymous reviewers.

References

- Adalsteinsson, D., & Sethian, J. A. (1999). The fast construction of extension velocities in level set methods. *Journal of Computational Physics*, *148*(1), 2–22.
- Adams, C. J., Iverson, N. R., Helanow, C., Zoet, L. K., & Bate, C. E. (2021). Softening of temperate ice by interstitial water. *Frontiers in Earth Science*, *9*, 702761.
- Andreassen, K., & Winsborrow, M. (2009). Signature of ice streaming in bjørnøyrenna, polar north atlantic, through the pleistocene and implications for ice-stream dynamics. *Annals of Glaciology*, *50*(52), 17–26.
- Bamber, J. L., Layberry, R. L., & Gogineni, S. (2001). A new ice thickness and bed data set for the greenland ice sheet: 1. measurement, data reduction, and errors. *Journal of Geophysical Research: Atmospheres*, *106*(D24), 33773–33780.
- Barnes, P., Tabor, D., & Walker, J. (1971). The friction and creep of polycrystalline ice. *Proceedings of the Royal Society of London. A. Mathematical and Physical Sciences*, *324*(1557), 127–155.
- Bindschadler, R. (2006). The environment and evolution of the west antarctic ice sheet: setting the stage. *Philosophical Transactions of the Royal Society A: Mathematical, Physical and Engineering Sciences*, *364*(1844), 1583–1605.
- Bingham, R. G., & Siegert, M. J. (2007). Radar-derived bed roughness characterization of institute and möller ice streams, west antarctica, and comparison with siple coast ice streams. *Geophysical Research Letters*, *34*(21).
- Bueler, J., Ed Brown. (2009). Shallow shelf approximation as a “sliding law” in a thermomechanically coupled ice sheet model. *Journal of Geophysical Research: Earth Surface*, *114*(F3).
- Carsey, F., Behar, A., Lane, A. L., Realmuto, V., & Engelhardt, H. (2002). A borehole camera system for imaging the deep interior of ice sheets. *Journal of Glaciology*, *48*(163), 622–628.
- Christoffersen, P., & Tulaczyk, S. (2003). Thermodynamics of basal freeze-on: predicting basal and subglacial signatures of stopped ice streams and interstream ridges. *Annals of Glaciology*, *36*, 233–243.
- Clarke, G. K. (1987). Fast glacier flow: Ice streams, surging, and tidewater glaciers. *Journal of Geophysical Research: Solid Earth*, *92*(B9), 8835–8841.
- Clarke, G. K., Nitsan, U., & Paterson, W. (1977). Strain heating and creep instability in glaciers and ice sheets. *Reviews of Geophysics*, *15*(2), 235–247.
- DiPrinzio, C., Wilen, L. A., Alley, R., Fitzpatrick, J., Spencer, M., & Gow, A. (2005). Fabric and texture at siple dome, antarctica. *Journal of Glaciology*, *51*(173), 281–290.
- Doyle, S. H., Hubbard, B., Christoffersen, P., Young, T. J., Hofstede, C., Bougamont, M., et al. (2018). Physical conditions of fast glacier flow: 1. measurements from boreholes drilled to the bed of store glacier, west greenland. *Journal of Geophysical Research: Earth Surface*, *123*(2), 324–348.
- Echelmeyer, K., & Zhongxiang, W. (1987). Direct observation of basal sliding and deformation of basal drift at sub-freezing temperatures. *Journal of Glaciology*, *33*(113), 83–98.
- Fowler, (2001). Modelling the flow of glaciers and ice sheets. In *Continuum mechanics and applications in geophysics and the environment* (pp. 201–221). Springer.
- Fowler. (2010). Weertman, liboutry and the development of sliding theory. *Journal of Glaciology*, *56*(200), 965–972.
- Franke, S., Jansen, D., Beyer, S., Neckel, N., Binder, T., Paden, J., & Eisen, O. (2021). Complex basal conditions and their influence on ice flow at the onset of the northeast greenland ice stream. *Journal of Geophysical Research: Earth Surface*, *126*(3), e2020JF005689.
- Glen. (1952). Experiments on the deformation of ice. *Journal of Glaciology*, *2*(12), 111–114.

- 805 Glen. (1955). The creep of polycrystalline ice. *Proceedings of the Royal Society of*
806 *London. Series A. Mathematical and Physical Sciences*, 228(1175), 519–538.
- 807 Goldsby, D., & Kohlstedt, D. L. (2001). Superplastic deformation of ice: Exper-
808 imental observations. *Journal of Geophysical Research: Solid Earth*, 106(B6),
809 11017–11030.
- 810 Goodwin, I. D. (1993). Basal ice accretion and debris entrainment within the coastal
811 ice margin, law dome, antarctica. *Journal of Glaciology*, 39(131), 157–166.
- 812 Gow, A., Epstein, S., & Sheehy, W. (1979). On the origin of stratified debris in ice
813 cores from the bottom of the antarctic ice sheet. *Journal of Glaciology*, 23(89),
814 185–192.
- 815 Gudmundsson, G. H. (1997). Basal-flow characteristics of a non-linear flow sliding
816 frictionless over strongly undulating bedrock. *Journal of Glaciology*, 43(143),
817 80–89.
- 818 Harrington, J. A., Humphrey, N. F., & Harper, J. T. (2015). Temperature distribu-
819 tion and thermal anomalies along a flowline of the greenland ice sheet. *Annals*
820 *of Glaciology*, 56(70), 98–104.
- 821 Helanow, C., Iverson, N. R., Woodard, J. B., & Zoet, L. K. (2021). A slip law for
822 hard-bedded glaciers derived from observed bed topography. *Science Advances*,
823 7(20), eabe7798.
- 824 Helanow, C., Iverson, N. R., Zoet, L. K., & Gagliardini, O. (2020). Sliding relations
825 for glacier slip with cavities over three-dimensional beds. *Geophysical Research*
826 *Letters*, 47(3), e2019GL084924.
- 827 Hermann, E., & Barclay, K. (1998). Basal sliding of ice stream b, west antarctica.
828 *Journal of Glaciology*, 44(147), 223–230.
- 829 Herron, S., Langway, C. C., et al. (1979). The debris-laden ice at the bottom of the
830 greenland ice sheet. *Journal of Glaciology*, 23(89), 193–207.
- 831 Hills, B. H., Harper, J. T., Humphrey, N. F., & Meierbachtol, T. W. (2017). Mea-
832 sured horizontal temperature gradients constrain heat transfer mechanisms in
833 greenland ice. *Geophysical Research Letters*, 44(19), 9778–9785.
- 834 Hoffman, M., & Price, S. (2014). Feedbacks between coupled subglacial hydrology
835 and glacier dynamics. *Journal of Geophysical Research: Earth Surface*, 119(3),
836 414–436.
- 837 Hunter, P., Meyer, C., Minchew, B., Haseloff, M., & Rempel, A. (2021). Ther-
838 mal controls on ice stream shear margins. *Journal of Glaciology*, 67(263), 435–
839 449.
- 840 Joughin, I., Rignot, E., Rosanova, C. E., Lucchitta, B. K., & Bohlander, J. (2003).
841 Timing of recent accelerations of pine island glacier, antarctica. *Geophysical*
842 *Research Letters*, 30(13).
- 843 Joughin, I., Smith, B., Howat, I., & Scambos, T. (2015). *Measures greenland ice*
844 *sheet velocity map from insar data, version 2*. NASA National Snow and Ice
845 Data Center Distributed Active Archive Center. Retrieved from [https://](https://nsidc.org/data/NSIDC-0478/versions/2)
846 nsidc.org/data/NSIDC-0478/versions/2 doi: 10.5067/OC7B04ZM9G6Q
- 847 Joughin, I., Smith, B. E., Howat, I. M., Scambos, T., & Moon, T. (2010). Green-
848 land flow variability from ice-sheet-wide velocity mapping. *Journal of Glaciol-*
849 *ogy*, 56(197), 415–430.
- 850 Karlsson, N. B., Solgaard, A. M., Mankoff, K. D., Gillet-Chaulet, F., MacGregor,
851 J. A., Box, J. E., et al. (2021). A first constraint on basal melt-water produc-
852 tion of the greenland ice sheet. *Nature Communications*, 12(1), 3461.
- 853 King, E. C., Hindmarsh, R. C., & Stokes, C. (2009). Formation of mega-scale glacial
854 lineations observed beneath a west antarctic ice stream. *Nature Geoscience*,
855 2(8), 585–588.
- 856 Krabbendam, M. (2016). Sliding of temperate basal ice on a rough, hard bed:
857 creep mechanisms, pressure melting, and implications for ice streaming. *The*
858 *Cryosphere*, 10(5), 1915–1932.

- 859 Kreiss, H.-O. (1968). Stability theory for difference approximations of mixed initial
860 boundary value problems. i. *Mathematics of Computation*, 22(104), 703–714.
- 861 Larson, F. . (1980). The uniqueness of steady state flows of glaciers and ice sheets.
862 *Geophysical Journal International*, 63(2), 333–345.
- 863 Law, R., Christoffersen, P., MacKie, E., Cook, S., Haseloff, M., & Gagliardini, O.
864 (2023). Complex motion of greenland ice sheet outlet glaciers with basal
865 temperate ice. *Science Advances*, 9(6), eabq5180.
- 866 Lliboutry, L. (1968). General theory of subglacial cavitation and sliding of temperate
867 glaciers. *Journal of Glaciology*, 7(49), 21–58.
- 868 Lüthi, M., Funk, M., Iken, A., Gogineni, S., & Truffer, M. (2002). Mechanisms of
869 fast flow in jakobshavn isbræ, west greenland: Part iii. measurements of ice
870 deformation, temperature and cross-borehole conductivity in boreholes to the
871 bedrock. *Journal of Glaciology*, 48(162), 369–385.
- 872 MacAyeal, D. R. (1989). Large-scale ice flow over a viscous basal sediment: Theory
873 and application to ice stream b, antarctica. *Journal of Geophysical Research:
874 Solid Earth*, 94(B4), 4071–4087.
- 875 Maier, N., Humphrey, N., Harper, J., & Meierbachtol, T. (2019). Sliding domi-
876 nates slow-flowing margin regions, greenland ice sheet. *Science Advances*, 5(7),
877 eaaw5406.
- 878 Mantelli, E., Haseloff, M., & Schoof, C. (2019). Ice sheet flow with thermally acti-
879 vated sliding. part 1: the role of advection. *Proceedings of the Royal Society A*,
880 475(2230), 20190410.
- 881 Maule, C. F., Purucker, M. E., Olsen, N., & Mosegaard, K. (2005). Heat
882 flux anomalies in antarctica revealed by satellite magnetic data. *Science*,
883 309(5733), 464–467.
- 884 Mellor, M., & Testa, R. (1969). Effect of temperature on the creep of ice. *Journal of
885 Glaciology*, 8(52), 131–145.
- 886 Meyer, C. R., & Creyts, T. T. (2017). Formation of ice eddies in subglacial moun-
887 tain valleys. *Journal of Geophysical Research: Earth Surface*, 122(9), 1574–
888 1588.
- 889 Meyer, C. R., & Minchew, B. M. (2018). Temperate ice in the shear margins of the
890 antarctic ice sheet: Controlling processes and preliminary locations. *Earth and
891 Planetary Science Letters*, 498, 17–26.
- 892 Minchew, B. M., & Meyer, C. R. (2020). Dilation of subglacial sediment governs incip-
893 ient surge motion in glaciers with deformable beds. *Proceedings of the Royal
894 Society A*, 476(2238), 20200033.
- 895 Morlighem, M., Williams, C. N., Rignot, E., An, L., Arndt, J. E., Bamber, J. L., et
896 al. (2017). Bedmachine v3: Complete bed topography and ocean bathymetry
897 mapping of greenland from multibeam echo sounding combined with mass
898 conservation. *Geophysical Research Letters*, 44(21), 11–051.
- 899 Mougnot, J., Rignot, E., & Scheuchl, B. (2014). Sustained increase in ice discharge
900 from the amundsen sea embayment, west antarctica, from 1973 to 2013. *Geo-
901 physical Research Letters*, 41(5), 1576–1584.
- 902 Nye. (1959). The motion of ice sheets and glaciers. *Journal of Glaciology*, 3(26),
903 493–507.
- 904 Nye. (1969). A calculation on the sliding of ice over a wavy surface using a new-
905 tonian viscous approximation. *Proceedings of the Royal Society of London. A.
906 Mathematical and Physical Sciences*, 311(1506), 445–467.
- 907 Nye. (1971). Causes and mechanics of glacier surges: discussion. *Canadian Journal
908 of Earth Sciences*, 8(2), 306–307.
- 909 Orlanski, I. (1976). A simple boundary condition for unbounded hyperbolic flows.
910 *Journal of Computational Physics*, 21(3), 251–269.
- 911 Osher, S., Fedkiw, R., & Piechor, K. (2004). Level set methods and dynamic implicit
912 surfaces. *Applied Mechanics Reviews*, 57(3), B15–B15.
- 913 Osher, S., & Sethian, J. A. (1988). Fronts propagating with curvature-dependent

- 914 speed: Algorithms based on hamilton-jacobi formulations. *Journal of Compu-*
 915 *tational Physics*, 79(1), 12–49.
- 916 Paterson, W. S. B. (1994). *Physics of glaciers*. Butterworth-Heinemann.
- 917 Peskin. (1972). *Flow patterns around heart valves: a digital computer method for*
 918 *solving the equations of motion*. Yeshiva University.
- 919 Peskin. (2002). The immersed boundary method. *Acta Numerica*, 11, 479–517.
 920 Retrieved from <https://doi.org/10.1080/00207540701450013> doi: doi:10
 921 .1017/S0962492902000077
- 922 Petrat, N., Zhu, H., Stadler, G., Hughes, T. J., & Ghattas, O. (2012). An inexact
 923 gauss-newton method for inversion of basal sliding and rheology parameters in
 924 a nonlinear stokes ice sheet model. *Journal of Glaciology*, 58(211), 889–903.
- 925 Pettit, E. C., Waddington, E. D., Harrison, W. D., Thorsteinsson, T., Elsberg, D.,
 926 Morack, J., & Zumberge, M. A. (2011). The crossover stress, anisotropy and
 927 the ice flow law at siple dome, west antarctica. *Journal of Glaciology*, 57(201),
 928 39–52.
- 929 Qin, Z., Delaney, K., Riaz, A., & Balaras, E. (2015). Topology preserving advection
 930 of implicit interfaces on cartesian grids. *Journal of Computational Physics*,
 931 290, 219–238.
- 932 Räss, L., Licul, A., Herman, F., Podladchikov, Y. Y., & Suckale, J. (2020). Mod-
 933 elling thermomechanical ice deformation using an implicit pseudo-transient
 934 method (fastice v1. 0) based on graphical processing units (gpu). *Geoscientific*
 935 *Model Development*, 13(3), 955–976.
- 936 Rempel, A. (2008). A theory for ice-till interactions and sediment entrainment be-
 937 neath glaciers. *Journal of Geophysical Research: Earth Surface*, 113(F1).
- 938 Rignot, E., & Mouginot, J. (2012). Ice flow in greenland for the international polar
 939 year 2008–2009. *Geophysical Research Letters*, 39(11).
- 940 Rignot, E., Mouginot, J., & Scheuchl, B. (2011). Ice flow of the antarctic ice sheet.
 941 *Science*, 333(6048), 1427–1430.
- 942 Rignot, E., Vaughan, D. G., Schmelztz, M., Dupont, T., & MacAyeal, D. (2002).
 943 Acceleration of pine island and thwaites glaciers, west antarctica. *Annals of*
 944 *Glaciology*, 34, 189–194.
- 945 Robin. (1955). Ice movement and temperature distribution in glaciers and ice sheets.
 946 *Journal of Glaciology*, 2(18), 523–532.
- 947 Ryser, C., Lüthi, M. P., Andrews, L. C., Hoffman, M. J., Catania, G. A., Hawley,
 948 R. L., et al. (2014). Sustained high basal motion of the greenland ice sheet
 949 revealed by borehole deformation. *Journal of Glaciology*, 60(222), 647–660.
- 950 Räss, L., Utkin, I., Duretz, T., Omlin, S., & Podladchikov, Y. Y. (2022, July).
 951 Assessing the robustness and scalability of the accelerated pseudo-transient
 952 method. *Geoscientific Model Development*, 15(14), 5757–5786. Retrieved 2022-
 953 10-19, from <https://gmd.copernicus.org/articles/15/5757/2022/> doi:
 954 10.5194/gmd-15-5757-2022
- 955 Schmid, D. W., & Podladchikov, Y. Y. (2003). Analytical solutions for deformable
 956 elliptical inclusions in general shear. *Geophysical Journal International*,
 957 155(1), 269–288.
- 958 Schoof, C. (2005). The effect of cavitation on glacier sliding. *Proceedings of the*
 959 *Royal Society A: Mathematical, Physical and Engineering Sciences*, 461(2055),
 960 609–627.
- 961 Schoof, C., & Mantelli, E. (2021). The role of sliding in ice stream formation. *Pro-*
 962 *ceedings of the Royal Society A*, 477(2248), 20200870.
- 963 Sethian, J. A. (1999). *Level set methods and fast marching methods: evolving in-*
 964 *terfaces in computational geometry, fluid mechanics, computer vision, and*
 965 *materials science* (Vol. 3). Cambridge university press.
- 966 Sethian, J. A., & Smereka, P. (2003). Level set methods for fluid interfaces. *Annual*
 967 *Review of Fluid Mechanics*, 35(1), 341–372.
- 968 Shapiro, N. M., & Ritzwoller, M. H. (2004). Inferring surface heat flux distributions

- 969 guided by a global seismic model: particular application to antarctica. *Earth*
 970 *and Planetary Science Letters*, 223(1-2), 213–224.
- 971 Siebert, M. J., Taylor, J., Payne, A. J., & Hubbard, B. (2004). Macro-scale bed
 972 roughness of the siple coast ice streams in west antarctica. *Earth Surface Pro-*
 973 *cesses and Landforms: The Journal of the British Geomorphological Research*
 974 *Group*, 29(13), 1591–1596.
- 975 Suckale, J., Platt, J. D., Perol, T., & Rice, J. R. (2014). Deformation-induced melt-
 976 ing in the margins of the west antarctic ice streams. *Journal of Geophysical*
 977 *Research: Earth Surface*, 119(5), 1004–1025.
- 978 Uhlmann, M. (2005). An immersed boundary method with direct forcing for the
 979 simulation of particulate flows. *Journal of Computational Physics*, 209(2),
 980 448–476.
- 981 Weertman, J. (1957). On the sliding of glaciers. *Journal of Glaciology*, 3(21), 33–
 982 38.
- 983 Whillans, I., Bolzan, J., & Shabtaie, S. (1987). Velocity of ice streams b and c,
 984 antarctica. *Journal of Geophysical Research: Solid Earth*, 92(B9), 8895–8902.
- 985 Wright, A., Young, D., Roberts, J., Schroeder, D., Bamber, J., Dowdeswell, J., ...
 986 others (2012). Evidence of a hydrological connection between the ice divide
 987 and ice sheet margin in the aurora subglacial basin, east antarctica. *Journal of*
 988 *Geophysical Research: Earth Surface*, 117(F1).
- 989 Yuen, D. A., & Schubert, G. (1979). The role of shear heating in the dynamics of
 990 large ice masses. *Journal of Glaciology*, 24(90), 195–212.

991 Appendix A Scaling of energy equation

992 To identify the relative magnitude of the terms in energy equation (9), we carry
 993 out a scaling analysis. We choose the characteristic parameters to be

$$994 \quad \bar{z} = H, \quad \bar{\tau} = \rho_i g L_z \alpha, \quad \bar{u} = U_s, \quad \bar{T} = T_0, \quad \bar{\epsilon} = \frac{U_s}{H}, \quad (\text{A1})$$

995 where $H = 1000$ m is the characteristic ice thickness, $U_s = 100$ m/yr is the charac-
 996 teristic surface speed, $T_0 = -26^\circ\text{C}$ is a typical atmospheric temperature in Antarctica,
 997 $\alpha = 2^\circ$ is the characteristic bed slope. Other relevant constants are: specific heat of
 998 ice $c_p = 2096.9$ J/(kg · K), ice density $\rho_i = 900$ kg/m³, thermal conductivity $\kappa = 2.51$ W/(m · K).
 999 As a characteristic vertical speed (or thinning speed), we assume the $U_t \sim U_s \times 10^{-2}$.
 1000 Substitute in the characteristic values and the constants, we have the scalings of the spa-
 1001 tial terms

$$1002 \quad \rho c_p \left(u_i \frac{\partial T}{\partial x_i} \right) \sim \mathcal{O}(10^{-3}), \quad \frac{\partial}{\partial x_i} \left(\kappa \frac{\partial T}{\partial x_i} \right) \sim \mathcal{O}(10^{-5}), \quad \tau_E \dot{\epsilon}_E \sim \mathcal{O}(10^{-3}). \quad (\text{A2})$$

1003 Note that in our problem setting of a slab of ice flowing down a slope, the domi-
 1004 nant shear strain rate is the shear strain rate $\dot{\epsilon}_{xz}$ and the dominant advection is the ver-
 1005 tical advection $U_t(\partial T/\partial z)$.

1006 Appendix B Scaling of momentum equation

1007 Assume a generic power-law rheology without temperature dependence, and also
 1008 assume that the dominant strain rate in the basal region is the shear strain rate. The
 1009 viscosity can be then expressed as

$$\eta = \frac{1}{2} a_0^{-\frac{1}{n}} \left(\frac{\partial u}{\partial z} \right)^{-1 + \frac{1}{n}}. \quad (\text{B1})$$

1010 Substitute in the viscosity, the x momentum equation 35 is

$$\eta \frac{\partial^2 u}{\partial x^2} + \frac{1}{n} \eta \frac{\partial^2 u}{\partial z^2} = \rho g \alpha, \quad (\text{B2})$$

$$\frac{\partial^2 u}{\partial x^2} + \frac{1}{n} \frac{\partial^2 u}{\partial z^2} = 2a_0^{\frac{1}{n}} \left(\frac{\partial u}{\partial z} \right)^{1-\frac{1}{n}} \rho g \alpha. \quad (\text{B3})$$

1011 Assume the characteristic horizontal length l . For the sinusoidal topography, we
 1012 consider l to be $\sim \lambda^{(n-1)p} k A^{1-(n-1)p}$, where p is some constant and n is the power-low
 1013 exponent. We choose $(n-1)$ to avoid zero denominator in the later derivation. Finally
 1014 the x momentum equation can be expressed as

$$\left(\frac{1}{l^2} + \frac{1}{n} \frac{1}{B_w^2} \right) = C \frac{1}{B_w^{1-\frac{1}{n}}}, \quad (\text{B4})$$

1015 where $C = 2\rho g \alpha a_0^{\frac{1}{n}} u^{-\frac{1}{n}}$. Simplify the equation, we have the following relationship

$$B_w^2 - Cl^2 B_w^{\frac{1}{n}+1} + \frac{l^2}{n} = 0 \quad (\text{B5})$$

$$l^2 = \frac{n B_w^2}{C n B_w^{\frac{1}{n}+1} - 1} \quad (\text{B6})$$

1016 Substitute representative numbers of $\rho = 900 \text{ kg/m}^3$, $g = 9.8 \text{ m/s}^2$, $a_0 \sim 10^{-10} -$
 1017 10^{-13} , $u \sim 100 \text{ m/yr}$, $B_w \sim 50 - 500 \text{ m}$, we have $C n B_w^{\frac{1}{n}+1} \sim 10^2 - 10^3$, thus the rela-
 1018 tionship between l and B_w can be further simplified to

$$l^2 = \frac{n B_w^2}{C n B_w^{\frac{1}{n}+1}} \quad (\text{B7})$$

$$B_w \propto l^{\frac{2n}{n-1}} \quad (\text{B8})$$

1019 We further substitute $Ak = 2\pi A/\lambda$, the above relationship can be alternatively
 1020 expressed as

$$B_w \propto (Ak)^{-2pn} \quad (\text{B9})$$

1021 Appendix C Velocity ratio distribution for different n and topogra- 1022 phies

1023 .

1024 .

1025 Figures C1 and C2 depict contour lines ranging from 15% to 95% of the surface
 1026 speed U_s , with each contour line spaced by 5% of U_s . When Ak is low, the velocity ra-
 1027 tio contours exhibit higher concentration around the peak region and a relatively more
 1028 evenly spaced distribution around the trough. This behavior indicates that the ice ex-
 1029 periences vertical compression and extension as it flows over basal topography. Further-
 1030 more, this observation suggests that the perturbations originating from the basal topog-
 1031 raphy propagate upwards from the bed to the surface over distances spanning tens to
 1032 several hundred meters. In contrast, when Ak is high, the velocity ratio contours tend
 1033 to concentrate at a consistent elevation and do not align with the shape of the basal to-
 1034 pography. Thus ice no longer experiences the alternation between vertical compression
 1035 and extension as flows downstream. This outcome implies that the actual form of the
 1036 basal topography exerts significantly less influence on the internal ice, and the flow be-
 1037 comes detached to a considerable extent from the true shape of the basal topography.

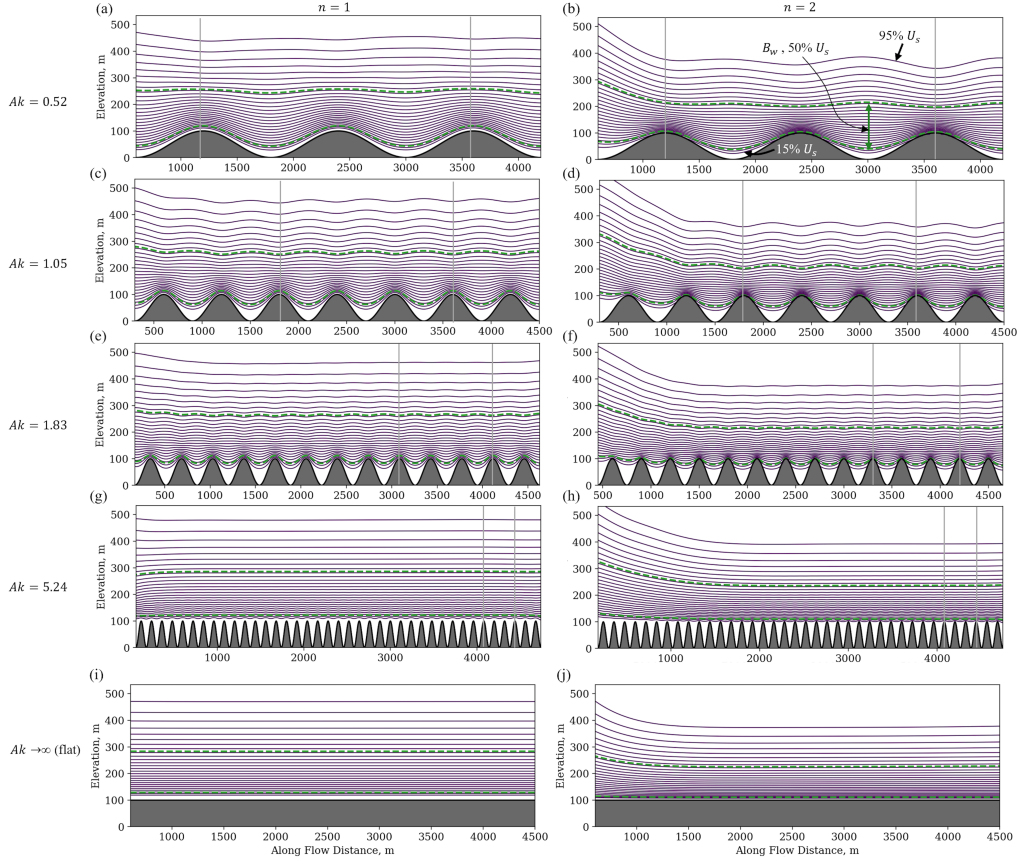


Figure C1. The velocity ratio (local x velocity divided by the surface x velocity in the same ice column) contours for $n = 1, 2$ and different Ak . Each row corresponds to a different shape factor: $Ak = 0.52, 1.05, 1.83, 5.24$, and ∞ (representing a flat bed). The first and second column represent the case where $n = 1$ and $n = 2$, respectively. In each panel, the purple lines show the contour lines from $95\%U_s$ to $15\%U_s$, with a separation of $3\%U_s$. The two green dashed lines represent the contour lines of $70\%U_s$ and $20\%U_s$, which define the internal shear band upper and lower bounds. Grey vertical lines indicate the spatial x locations where we calculate the average internal shear bandwidth.

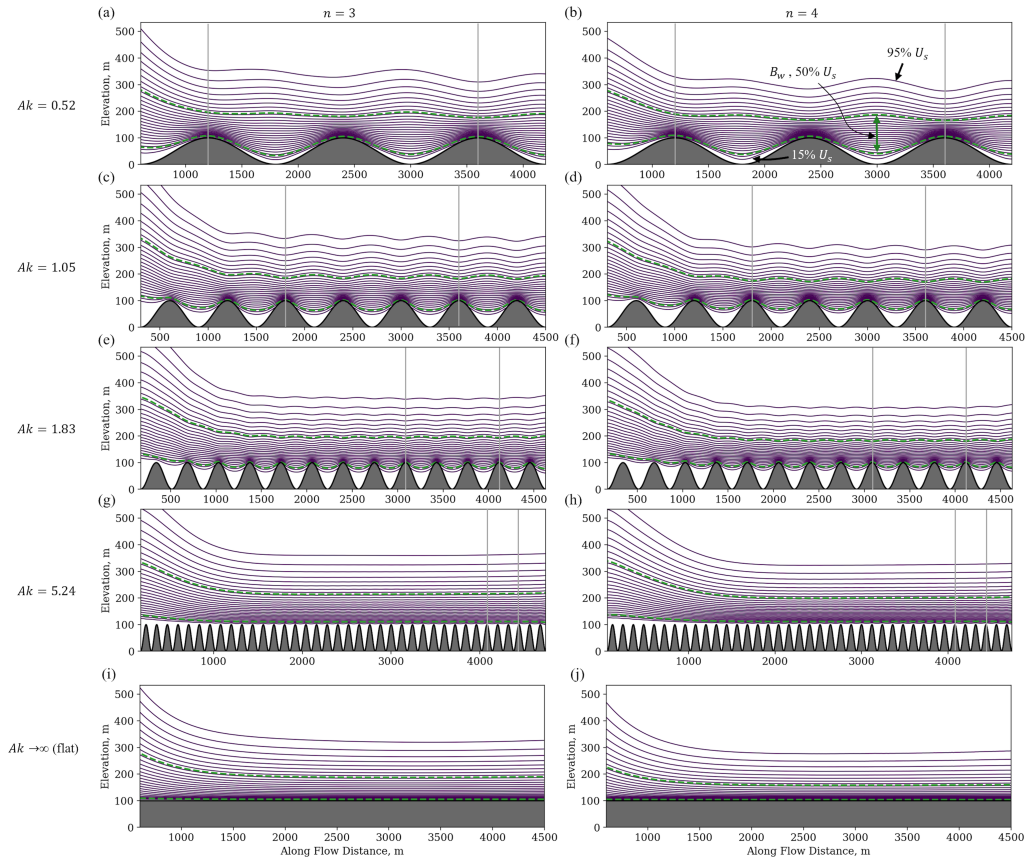


Figure C2. The velocity ratio contours for different $n = 3, 4$ and different Ak . The layout of this figure follows the same as Figure C1